

Uwe Hergenhan

**Photoionisation von Molekülen und Clustern
an einer Synchrotronstrahlungsquelle der
dritten Generation**

Photoionization of
Molecules and Clusters at a
Third Generation Synchrotron Radiation Source

Photoionization of Molecules and Clusters at a Third Generation Synchrotron Radiation Source

Uwe Hergenhahn

Max-Planck-Institut für Plasmaphysik, Boltzmannstr. 2, 85748 Garching

Abstract. Photoionization experiments on free molecules and clusters carried out by the author are reviewed. Vibrationally resolved photoelectron spectroscopy with an instrumental resolution below the lifetime broadening has been performed on the core levels of small C, N, and O containing molecules. Subtle details of the interplay between vibrational and electronic structure have been revealed. Probing the carbon core levels of chiral, somewhat larger molecules with circularly polarized synchrotron radiation shows a circular dichroism in the photoelectron angular distribution, which is present even for non-oriented molecular samples. More details on photoionization processes can be revealed by coincidence experiments. Energy spectra of oxygen resonant Auger electrons taken with high resolution and with kinematical reconstruction of the molecular axis directions show clear signatures for intramolecular electron scattering and electron transfer. Photoelectron spectroscopy of clusters at photon energies larger than the He I α line has rarely been carried out so far. First experiments have proven the existence of a non-local autoionization process – Interatomic Coulombic Decay – which involves cooperative transitions at two different sites of a weakly bonded system.

Contents

1	Introduction	3
2	Experimental setup	5
2.1	Experimental arrangement at the NSLS	5
2.2	Experimental arrangement at BESSY	6
2.2.1	High-resolution photoelectron spectroscopy	7
2.2.2	Dichroism measurements	8
2.2.3	Experiments on clusters	9
2.2.4	Electron-ion and electron-electron coincidence setups	10
3	Vibrational structure in inner shell photoionization of molecules	14
3.1	Theory of vibrational excitation by photoionization	14
3.2	Vibrationally resolved photoelectron spectra	15
3.2.1	Methane - CH ₄	15
3.2.2	Nitrogen - N ₂	18
3.2.3	Carbon Dioxide - CO ₂	22
4	Photoelectron circular dichroism in chiral molecules	24
4.1	Sign conventions	24
4.2	Theory of photoelectron circular dichroism	25
4.3	Photoelectron circular dichroism in C 1s photoemission of camphor . . .	26
4.4	Photoelectron circular dichroism in C 1s photoemission of carvone . . .	31
4.5	Summary	32
5	Interatomic Coulombic Decay in weakly bonded systems	33
5.1	The Interatomic/Intermolecular Coulombic Decay Process	34
5.2	ICD spectra of Ne clusters	35
5.3	ICD spectra of NeAr heteroclusters	38
5.4	Discussion and Summary	40
6	Electron-ion coincidence spectroscopy with high energy resolution	42
6.1	Intramolecular electron scattering and electron transfer in oxygen	43
7	Outlook	47

1. Introduction

The use of photoionization as a probe to investigate matter dates back to the beginning of the last century. Results on photoionization of inner shells of molecules, excited with soft X-radiation, earned Kai Siegbahn the Nobel prize in 1981. Since then, technology for the production of vacuum ultraviolet and soft X-radiation has quickly developed and today far more sophisticated experiments are possible. In this work I will describe results of photoionization studies, most of which have been carried out within the last five years at the third generation synchrotron radiation source BESSY II. These experiments make full use of the spectral purity and the versatile polarization type of the radiation, which in this spectral range has not been achieved earlier.

After an experimental section this review describes experiments on the vibrational excitation of molecules by inner shell photoionization, with an emphasis on the coupling of vibrational and electronic structure, hitherto hardly explored for this class of states. More details on some aspects of the apparatus can be found in the references [11] and [12].‡ Results for highly resolved inner shell photoelectron spectra are covered extensively in ref. [7]. Some interesting original material was published in [20].

The following section extends inner shell photoionization to chiral molecules, studied with circularly polarized light. Here, besides the conventional circular dichroism in absorption, which is well known in the visible region, a new type of dichroism is possible, which is observed as an asymmetry of the differential partial photoionization cross sections. Contrary to circular dichroism in absorption, this new effect may already occur in the electric dipole approximation. I will further discuss it as ‘photoelectron circular dichroism’. This chapter is based on ref. [9], and also gives some introductory information that was not included in the publication.

Another important aspect in photoionization studies of highly excited electronic states are secondary processes. While among these Auger decay is well known, it has only recently been recognized that in weakly bonded systems another type of autoionization process is possible, the so-called Interatomic or Intermolecular Coulombic Decay (ICD), which requires less excitation energy and is only viable due to participation of the chemical environment of the initially excited site. I will outline the theory of ICD, with an emphasis on the distinctions from Auger decay, and will show results on Ne clusters, which gave the first experimental proof of this phenomenon, originally reported in publications [4] and [13]. The influence of the environment on the ICD process was studied by us in NeAr heteroclusters, for which very recent unpublished data are shown.

Finally, more sophisticated studies of the dynamics of photoionization and its subsequent processes are possible by electron-ion coincidence detection techniques. As a demonstration of the prospects of such experiments with high energy resolution, results for resonant Auger emission from dissociating oxygen molecules are presented. A significant fraction of the resonant Auger electrons are emitted after dissociation of the

‡ These, and all other references mentioned explicitly in the introduction, are included as reprints at the end of this review.

molecule, that is already in the atomic region. As reported in ref. [6], we show that these can undergo scattering on the other, neutral fragment atom and that electron transfer between the two fragments is possible even after dissociation.

This review aims at giving an introduction into the photoionization experiments of the author. Complementary to this work, a review article on vibrational excitation in inner shell photoionization by the author has recently appeared [7]. References to my own work are given in square brackets, and refer to the full publication list starting on page 51. References to other works are given in Harvard notation.

2. Experimental setup

In this section I will describe properties of our setup for photoelectron spectroscopy at the Berliner Elektronenspeicherring für Synchrotronstrahlung (BESSY) that are relevant for the experiments covered in this work. Some early experiments in this work have been done with another setup at the National Synchrotron Light Source (NSLS) in Brookhaven, NY, which is also described.

2.1. Experimental arrangement at the NSLS

From 1996 to 1999 experiments were carried out at the high energy electron storage ring of the NSLS. The soft X-ray undulator X1 of this facility has been constructed to serve interests of a number of groups active in X-ray microscopy and photoelectron spectroscopy. This device is a 35-pole, hybrid type undulator of 8.0 cm period length (Buckley *et al* 1989) (see table 1). The beam divergence at the NSLS however is too large to allow operation of the device as a true undulator, which is recognized by the huge width of the harmonics and the occurrence of even harmonics with a considerable intensity.

Because of the large divergence, it was possible to split the beam of X1 to allow simultaneous operation of two monochromators serving different endstations. The spectroscopy branch X1B was constructed in 1991-2 by the Fritz-Haber-Institute Berlin jointly with groups from the Forschungszentrum Jülich and from Brookhaven National Laboratory. It is equipped with a Dragon type monochromator (Randall *et al* 1992). This comparatively simple design with two cylindrical focussing mirrors and a spherical grating was first successfully demonstrated at the NSLS. After an exchange of the grating in 1996, the useable photon resolution for inner shell photoelectron spectroscopy was 60 meV at the carbon K-edge, 80 meV at the nitrogen K-edge and 100 meV at the oxygen K-edge. Before third generation synchrotron radiation sources became operational, the X1B beamline was very competitive in terms of flux at high resolution in the soft X-ray range.

For photoelectron spectroscopy, a cylindrical mirror analyser (CMA) was used (Feldhaus *et al* 1992). Quite uniquely the axis of this instrument coincides with the photon beam, and electrons were collected under a backward scattering angle of 54.7° relative to the photon propagation direction. A spherical entrance lens allowed to oper-

Table 1. Electron beam parameters and undulator parameters for synchrotron radiation sources used in this work.

Insertion Device		Energy (GeV)	Number of Poles	Length (m)	Source Size $\sigma(h) \times \sigma(v)$ (μm)	Source Divergence $\sigma'(h) \times \sigma'(v)$ (μrad)
NSLS	X1B	2.8	35	2.80	300×6	260×35
BESSY II	U49	1.7	83	4.07	290×15	17×4

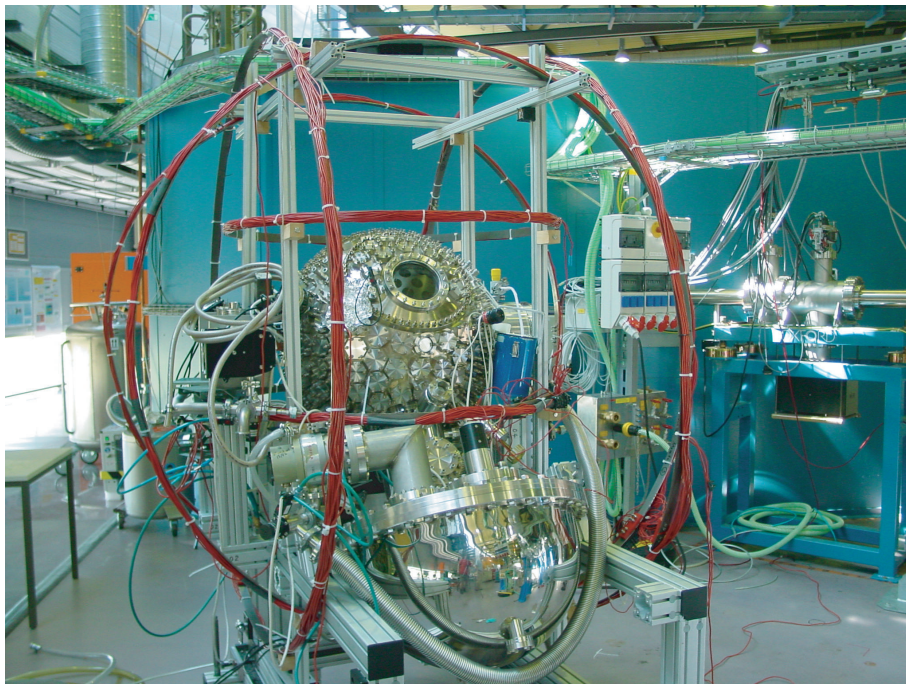


Figure 1. Photograph of the apparatus used for photoionization experiments at BESSY II. The spherical vacuum chamber including 240 DN-CF40 flanges for small time-of-flight electron detectors, the Scienta electron spectrometer and the Helmholtz coils used for compensation of magnet fields can be seen.

ate the instrument in a constant pass energy mode with pass energies down to 7.5 eV and a useable resolution of 80 meV. Electrons were collected by a set of microchannel plates with a central hole for the synchrotron radiation and a sectorized anode, which allowed to record total intensities and angular distribution parameters at the same time.

With this instrumentation, we have carried out a number of studies on molecular K-shell photoionization [14, 22–25, 29–37].

At the time the analyser was conceptually designed, the electric dipole approximation was believed to hold for photon energies below 1 keV. In recent years, however, a measurable effect of an electric dipole-electric quadrupole interference term in the photoionization amplitude was found for some molecules (Hemmers *et al* 2001). This term leads to a redistribution of photoelectron intensity between forward and backward scattering directions. To this extent, the angle integrated cross section measured in our CMA is not strictly proportional to the total cross section. This correction is discussed in some detail in [22] and [23], and typically amounts to less than 10 %.

2.2. Experimental arrangement at BESSY

In 1999 the high brilliance synchrotron radiation source BESSY II in Berlin opened for user operation. It was anticipated that this would lead to a significant improvement of experimental conditions, and therefore a new, versatile apparatus for photoionization ex-

periments was constructed (figure 1). I would like to discuss the properties of BESSY II as a photon source first.

This electron storage ring is dedicated to the production of synchrotron radiation by undulators. The main differences to older sites are the significantly smaller dimensions of the electron beam, which determines the source size of the synchrotron radiation, and the use of long undulators as the main devices for the production of synchrotron radiation. Because of these two characteristics, BESSY II and a number of similar synchrotron radiation sources have been termed ‘third generation’. For high photon resolution experiments at the inner shells of light elements, the U49 undulators are best suited. These have 83 periods of 4.9 cm length, leading to an overall length of 4.07 m. The progress in the operating conditions compared to the NSLS can best be seen by comparing the beam divergence in table 1. While the electron beam size in the central part of a straight section can be comparable at second and third generation sources, the beam diameter towards the ends of the section grows much more rapid in the former. These quantities directly determine the solid angle interval into which the synchrotron radiation is emitted. As a consequence, at third generation sources the focussing of the beam is improved, the useable experimental resolution is better and the spot size at the experiment is much smaller. Moreover, the undulator harmonics are less wide and therefore the intensity gain on the top of the harmonic is more pronounced. For the U49/1-SGM beamline, the useable photon resolution is better than 30 meV at the nitrogen K-edge [20]. Undulator beamlines at second generation sources can still be competitive if neither ultra high resolution nor small source sizes are required by the experiment. This can be seen by the similar values of the total photon flux at the nitrogen K-edge of approximately $10^{11}/\text{s}$ at the best reasonably useable settings of the resolution measured for both X1B (Randall *et al* 1992) and the U49/1-SGM (Senf *et al* 2001).

The heart of the endstation constructed for gas phase photoionization experiments at BESSY and at forthcoming free electron laser photon sources is a spherical vacuum chamber of 655 mm outer diameter. It is equipped with two removeable lids of diameter 355 mm, 4 DN 200 CF and 150 CF flanges, and 241 small flanges of size DN 40 CF. The latter allow experiments with electron time-of-flight spectrometers under any geometry, while by the 355 mm diameter flanges large supplemental equipment components can be fitted to the chamber. First experiments on electron-electron coincidences with short time-of-flight spectrometers and the construction of a supersonic molecular beam for production of cold molecules and clusters will be discussed in later sections of this work.

The main experimental chamber is isolated from the synchrotron radiation beamline by a two-stage differential pumping section, which is terminated at both ends by narrow capillaries.

2.2.1. High-resolution photoelectron spectroscopy For high resolution non-coincident photoelectron spectroscopy the apparatus is equipped with a large hemispherical electron analyzer (Scienta ES 200). Within the experimental chamber, the target is pro-

duced in a gas cell, which consists of a tube section of 38.1 mm outer diameter. The use of a gas cell is essential to increase the pressure of the target gas and to shield stray electric fields and stray electrons from the analyser. The synchrotron beam travels through the cell parallel to its rotation axis, but at a distance of 1-2 mm to the cell wall. At the wall of closest proximity to the beam, a slit of 10×1 mm extension and aligning with the photon beam is cut. Hence electrons do not travel for more than 1-2 mm through the increased pressure region of the gas cell. Further in that direction the hemispherical analyzer is placed at a downward angle of 54.7° relative to the horizontal, and in the plane perpendicular to the beam propagation axis. In this geometry, the lowest order multipole corrections to the electric dipole transition amplitude for photoionization vanish [22]. The design of the gas cell is of some importance to reach high electron energy resolution (Baltzer *et al* 1993). Our design includes electrodes for producing a small electrostatic field along the slit, which empirically improves the energy resolution in some situations, and an electron dump opposite to the slit for the electrons, which is essential to achieve clean spectra at low kinetic energies. The walls of the cell are coated with graphite.

The resolution limit of the analyser as demonstrated by ionization of a noble gas with a He discharge source is better than 10 meV. In experiments with synchrotron radiation, with this instrument we have achieved an energy resolution of 10 meV. The discrepancy to the He I results we attribute to imperfections of the magnetic field compensation by the Helmholtz coils shown in figure 1.

2.2.2. Dichroism measurements Photoelectron circular dichroism is a difference of energy and angle resolved photoelectron intensity depending on the handedness of circular polarization of the ionizing radiation. For the measurement of this effect, described in section 4, light of circular polarization is needed. In the VUV and soft X-ray range of wavelengths, phase-shifting elements for radiation are only available for a few, narrow wavelength intervals [21, 26, 27]. The production of circularly polarized radiation with a tunable wavelength currently is only possible at synchrotron radiation sources. In third generation storage rings, by suitable arrangements of permanent magnets electrons can be bent onto corkscrew-like trajectories, which leads to high circular polarization degrees. The elliptical undulators UE56/2 at BESSY employ this principle (Weiss *et al* 2001), and have been used for all experiments with circular polarization described here. The UE56/2 is a twin undulator, the two undulator structures of which can be set independently to produce radiation of different polarization. Rapid switching between the two beams is possible by a mechanical chopper. Since this option was commissioned in 2003, part of the experiments described here were done instead by repeated measurements with one undulator, which was subsequently set to opposite handedness of the circular polarization.

From the theory of photoelectron circular dichroism, this effect is expected to vanish in the plane perpendicular to the beam propagation axis (Ritchie 1976). For its measurement, the apparatus described above had to be used in a different geometry.

This was achieved by rotating the vacuum chamber and its frame by 90° , such as to place the hemispherical electron analyser in a forward scattering geometry with an angle of 54.7° relative to the photon beam.

The energy resolution of the analyser in these measurements is less important. Instead, it is essential to record spectra with opposite helicities of the radiation under essentially similar conditions. In the Scienta analyzer a multiplex readout is achieved by detecting the electrons at the end of the hemisphere on a microchannel plate of 50 mm nominal diameter. By this a band of electron energies within an interval around the nominal pass energy can be recorded in parallel. In the present experiments, the energy window was made sufficiently large to encompass all C 1s photoelectron lines of the molecule of interest by setting the pass energy to 75 eV. Thus, spectra were recorded without scanning the analyser voltages. Lately a mechanical chopper was commissioned that allowed to record spectra for 10-20 s, then switch helicity, and then record for the same amount of time with the other helicity. This procedure was repeated about 40-60 times to collect data with meaningful statistics. Before availability of the chopper, photoelectrons for a given photon energy were collected typically for ten minutes; then the light helicity was switched, and a spectrum with otherwise identical settings was recorded for the same amount of time. These pairs of spectra were recorded several times for every photon energy, and for both enantiomers.

2.2.3. Experiments on clusters The photoemission of weakly bound species, such as van-der-Waals clusters or hydrogen-bridge bonded clusters, has rarely been investigated at photon energies higher than what can be achieved with a He I discharge laboratory source. In order to start a project on these species, between 2001 and 2003 a coolable molecular beam source was fitted into the spherical vacuum chamber described above (see ref. [11]). In this source, clusters form by three-body collisions when the gas expands through a narrow nozzle into the vacuum. Our molecular beam source has a two-stage design: the gas is emitted into a so-called expansion chamber, then the central part of the beam is led through a small conical orifice, the ‘skimmer’, into the main experimental chamber. A schematic of this experimental setup is shown in figure 2.

Our major aim was to create a setup that is capable of recording electron spectra of high energy resolution, and down to kinetic energies of less than 1 eV. Therefore, all parts close to the interaction region had to be made of non-magnetic materials. To fit the setup into the existing experimental chamber, a compact design was required. The spatial constraints also limit the pumping capacity at the expansion chamber. To compensate for the limited pumping speed and the consequent limitations of stagnation pressure, it was necessary to implement an effective cooling mechanism to achieve nozzle temperatures down to 25 K for sufficient cluster production. To increase the thermal stability of the system an active temperature controlling unit (Scientific Instruments 9600) can be used.

In our experiments, copper nozzles with diameters of 80 μm to 200 μm have been used. The smaller nozzles seemed to lead to a somewhat better cluster production.

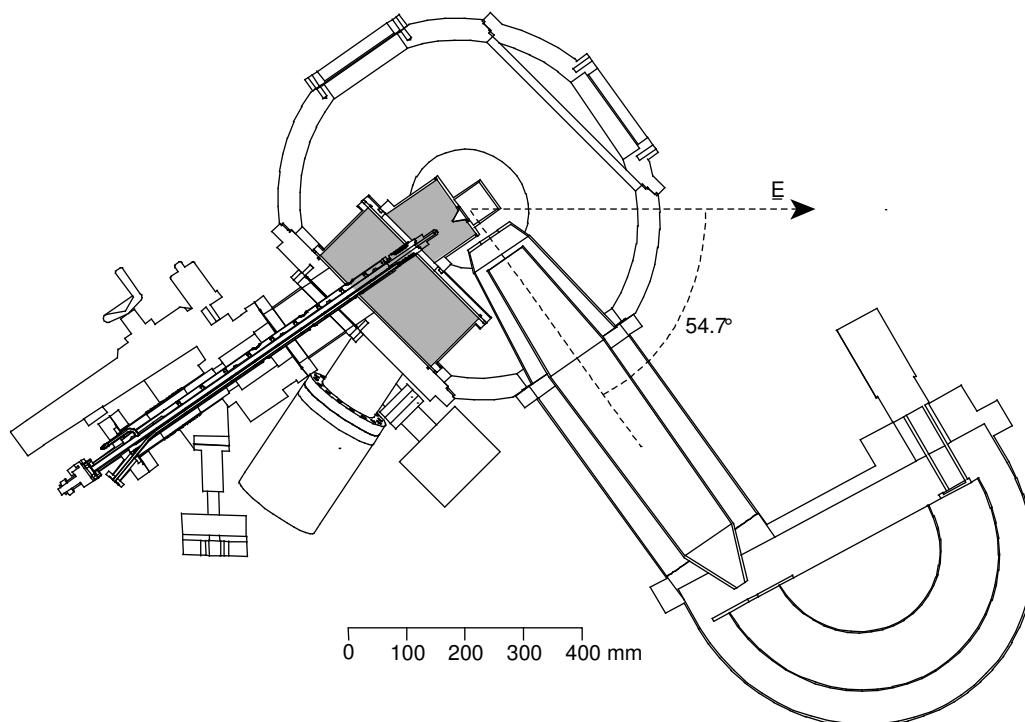


Figure 2. Spherical vacuum chamber and cluster source: The expansion compartment (grey shaded) extends into the chamber and is separated from the interaction region by a conical skimmer [11]. The cluster source is supported by a xyz-manipulator and can be cooled with liquid helium or liquid nitrogen. Also shown is one of the two turbo pumps at the expansion chamber and a pressure gauge at that pumping port. The photon beam is perpendicular to the drawing plane.

Using these with two 240 l/s turbo pumps at the expansion chamber, typical stagnation pressures reach 1.5 bar. The expansion chamber pressure then is in the 10^{-3} mbar range, and the pressure in the main chamber in the 10^{-6} mbar range. Clusters of Ne were produced with this setup at typical nozzle temperatures of 40 K, and clusters of various other atoms and molecules already form at higher temperatures.

2.2.4. Electron-ion and electron-electron coincidence setups Detailed information on a photon-induced process can be achieved by detecting several of the reaction products in coincidence. In its standard configuration, the Scienta spectrometer is not suitable for this type of experiment since its electron detector is read out by a video camera via a fluorescent screen. This technique is slow, and does not allow to uniquely connect the detection of a single electron to an event registered in another detector. In order to facilitate coincidence measurements we have therefore replaced the original microchannel plate (MCP) stack by a fast, position-sensitive anode based on the delay line principle (Roentdek, Frankfurt) (see ref. [12] and figure 3, panel a). The delay line anode consists of two pairs of parallel wires, which are wound on a quadratical frame that encompasses the full MCP area. Each pair spans between two opposing sides of the frame. A slight

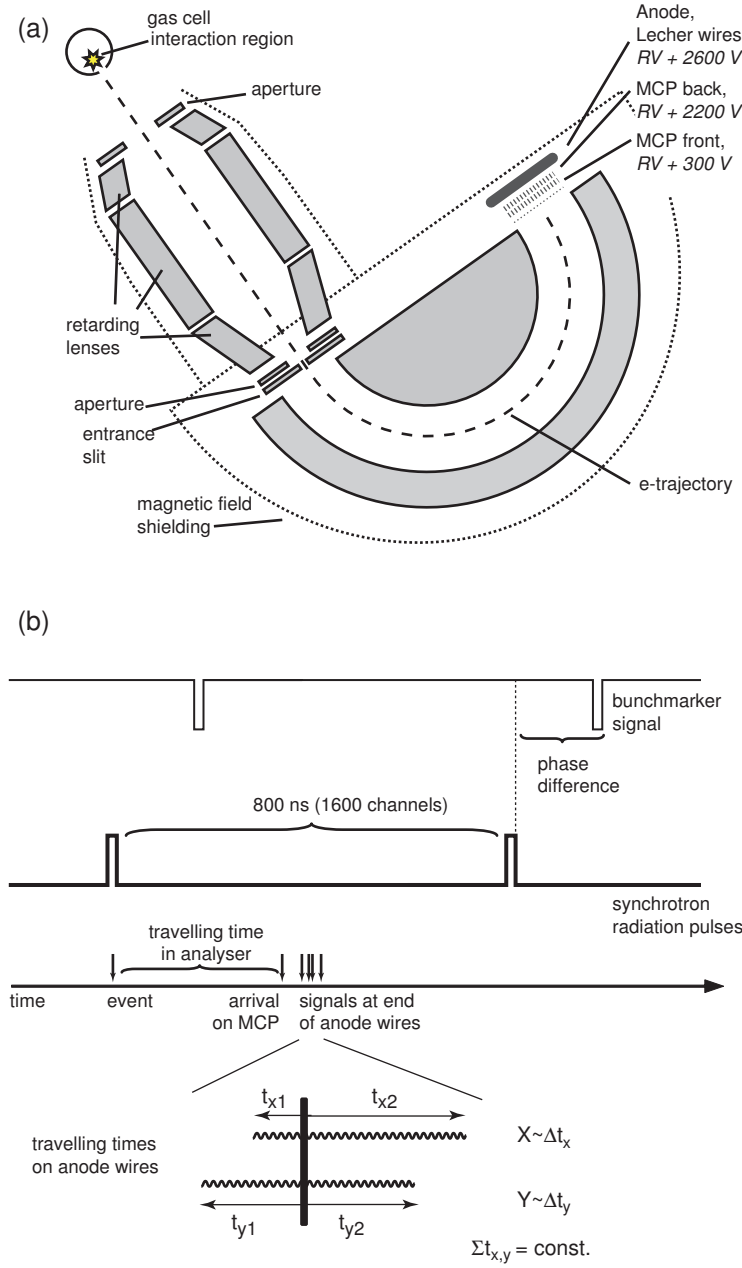


Figure 3. (a) Schematic of the modified hemispherical electron spectrometer [12]. A cut through the spectrometer is shown. Horizontally linearly polarized synchrotron radiation is directed perpendicular to the drawing plane, and the central entrance angle of electrons is the magic angle of 54.7° with respect to the horizontal. All voltages applied to the anode are floating on the retarding voltage (RV), *i.e.* the difference of the original kinetic energy and the selected pass energy. (b) Schematic of some time differences important in the experiment. In single bunch mode, synchrotron radiation pulses arrive at a repetition rate of 800 ns. After travelling in the analyser, an electron produced by a light pulse is detected by triggering a microchannel plate (MCP) signal. Subsequently, two pairs of pulses are generated on the anode wires. Their arrival time differences at the end of the wires (not drawn to scale) define the position coordinates of the pulse on the MCP. An electronic trigger signal ('bunchmarker') synchronized to the radiation pulses, but with some phase difference, is provided by the storage ring.

displacement in height is used to insulate the two pairs of wires from each other. An electron cloud produced by the second MCP leads to a voltage drop at each wire, which propagates in both directions. The setup of the wires as pairs (‘Lecher wires’) serves as a wave guide for the signals. By measuring the arrival times of the pulses at the ends of each wire pair and calculating their time difference, the position coordinates of the electron cloud can be determined (see figure 3, panel b). Since in this setup the main uncertainty for the detection time of an electron is given by path length differences of the trajectories through the hemispherical analyser, which translates to timing uncertainties in the order of ns, electron-electron and electron-ion coincidence measurements can be carried out.

The energy resolution of the analyser is influenced by the spatial resolution of the anode. The specification for the original CCD based setup is $100\ \mu\text{m}$, and a comparable value can be reached by using a delay line anode with difference amplifiers which produce trigger signals corresponding to the centroids of the voltage pulses coming from the Lecher wires, and sufficiently fast time-to-digital converters (TDC). In the experiment reported in ref. [12], the spatial resolution was still hampered by a TDC resolution of only 500 ps, while in later experiments with an upgraded TDC of 60 ps time resolution, an energy resolution equivalent to the original setup was achieved. After these experiments were reported, the manufacturer of the analyser decided to offer replacement of the conventional anode by a delay line detector as a commercially available upgrade.

Two different types of experiment have been facilitated by the detector replacement, namely photoelectron-Auger electron and photoelectron-ion coincidence measurements. In both experiments the capability for coincident detection of fast electrons (kinetic energies of several hundred eV) was used, which is not easily possible by other coincidence setups.

Photoelectron – Auger electron coincidences were detected by a combination of the Scienta spectrometer with two linear time-of-flight (TOF) detectors. Due to its superior resolution for high energy electrons, the Scienta was set to detect a portion of the Auger spectrum. The pertaining photoelectrons were recorded by the time-of-flight spectrometers. After initial setup of the apparatus in single bunch mode, this arrangement was used for coincident spectroscopy of electron pairs in multi bunch mode as well. Arrival times of electrons in all analysers were recorded relative to the BESSY bunch marker, and were supplemented by a unique bunch number received from a counter which is incremented by the bunch marker. The arrival of each electron was recorded separately for off-line data analysis. The event file resulting from these data can thus be searched for electron-electron coincidences in retrospect. The discrimination of random coincidences from true events is possible even in multi bunch mode, since the true coincidences occur at a fixed time difference between the two electrons detected in the Scienta and in the TOF. The rate of true coincidences amounted to 1 Hz. By this setup we have separated the N 1s K-VV Auger spectrum of N_2O into contributions from the terminal and the central nitrogen atom.

Photoelectron – photoion coincidences were recorded by placing a projecting ion

spectrometer (an improved version of the instrument described by Becker *et al* 2000) opposite to the electron spectrometer. Below the author will report on an experiment in which fast fragmenting excited states of O_2 were produced by excitation of a core electron to an antibonding valence shell. An ionic fragment was then detected in coincidence with a resonant Auger electron of roughly 500 eV kinetic energy (ref. [6] and section 6). This measurement was carried out at the U49/2-PGM1 beam line of BESSY operating in single bunch mode. Using a position resolving anode in the ion spectrometer together with a time-of-flight measurement of the ions enabled us to reconstruct all three components of the momentum vector \mathbf{k} of the ions at the instance of fragmentation. Since the use of static electric fields, common in many \mathbf{k} -resolving ion measurements, is not compatible with the needs of high electron energy resolution, the ion spectrometer is operated with a pulsed electric field triggered by the electron arrival. The ion time-of-flight spectrometer uses a position resolving detector with 10 ns multi hit capability. The electron analyzer was operated at a pass energy of 40 eV, resulting in an energy resolution better than 100 meV. All events were stored separately for off-line data analysis. Reconstruction of the ion momenta was done according to a look-up table produced by a numerical simulation of the ion trajectories.

3. Vibrational structure in inner shell photoionization of molecules

Photoionization probes the electronic structure of the ionic state. The resulting information can also be used to conclude on ground state properties. While the determination of ionization potentials yields the electronic energy levels, the determination of the vibrational fine-structure of a molecular photoelectron spectrum yields information on the potential surfaces and from these on the molecular geometry. Vibrational excitation in photoionization processes is driven by the change in geometry between initial state – here always the neutral ground state – and ionized state. Until the 1970s, inner-shell photoionization was not believed to produce a vibrational fine-structure, since core orbitals were seen as non bonding and by that a change in molecular geometry was not anticipated. The sudden removal of a core electron however acts on the remainder of the molecule like a sudden increase of the nuclear charge on the ionized site. The valence shell of the molecule adapts to this change, a process called relaxation. In many ionization processes relaxation entails significant changes in equilibrium geometry, although usually not as large as from ionizing a bonding or anti-bonding electron.

Experimental investigation of vibrational fine structure in inner shell photoionization necessitates high photon energy resolution and high kinetic energy resolution at high photon energies. Because of this, despite the conceptual simplicity of the experiments, the investigations reviewed here have been performed within the last five years, after third generation synchrotron radiation sources became available.

3.1. Theory of vibrational excitation by photoionization

Photoionization experiments in this work will be described within the Franck-Condon approximation, which states that the nuclear motion during the photoionization process itself can be neglected. A further approximation often used is the Born-Oppenheimer (BO) approximation, which states that the wavefunction of a molecule containing M nuclei with cartesian position coordinates $\mathbf{R}_k, k = 1, \dots, M$ and N electrons with coordinates $\mathbf{r}_l, l = 1, \dots, N$ can be written as $\Phi(\mathbf{r}; \mathbf{R})\chi(\mathbf{R})$. Here Φ is an electronic wavefunction, which only depends parametrically on all nuclear coordinates $\mathbf{R} = \{\mathbf{R}_1, \dots, \mathbf{R}_M\}$, and χ is a wavefunction that solves the nuclear Schrödinger equation (see *e.g.* ref. [7]). In a simple approximation, Φ can be an antisymmetrized product of Hartree-Fock molecular orbitals and χ a product of harmonic oscillator wavefunctions in all nuclear degrees of freedom. The validity of the Born-Oppenheimer approximation is closely related to the energy separation of the electronic states. An electronic state labelled i , the potential surface $V_i(\mathbf{R})$ of which is well separated from all other states, can be described by a single BO solution $\Phi_i(\mathbf{r}; \mathbf{R})\chi(\mathbf{R})$ to a good degree of accuracy. This is termed the adiabatic approximation.

The adiabatic approximation loses its validity at points in nuclear configuration space where potential surfaces of different electronic states intersect, or come in close energetical proximity. ‘Close’ in this context means a separation which is comparable to or smaller than the size of a vibrational quantum. At these points, the prerequisite

of the Born-Oppenheimer approximation, namely a smooth variation of the electronic wavefunctions with \mathbf{R} , is violated. The system then has eigenfunctions, which are mixtures of different electronic-vibrational states $\sum_{i,j} \Phi_i(\mathbf{r}; \mathbf{R}) \chi_j(\mathbf{R})$. This situation is termed vibronic (*vibrational-electronic*) coupling.

As long as the Franck-Condon approximation and the Born-Oppenheimer approximation are valid, only totally symmetric modes can be excited. By vibronic coupling, some or all of the vibrational intensity can be transferred to non-totally symmetric modes.

Independent of the validity of the adiabatic approximation, potential surfaces of most molecular ground and ionized states are not strictly harmonic. An improved shape for an oscillator in one coordinate R is given by the Morse potential, which can be written as

$$V(R) = D_0 \left[\left(1 - \exp(-\beta(R - R^{(0)})) \right)^2 - 1 \right]. \quad (1)$$

The constants D_0 and β have the dimensions of an energy and of an inverse length, and determine the depth and the ‘steepness’ of the potential curve. $R^{(0)}$ is the equilibrium configuration. The energy levels of an oscillator in a Morse potential are given by

$$E(n) = -D_0 + \hbar\omega(n + 1/2) - \hbar\omega x(n + 1/2)^2. \quad (2)$$

3.2. *Vibrationally resolved photoelectron spectra*

In the following, some examples of vibrationally resolved photoelectron spectra are presented. These have been recorded by the author at BESSY II under experimental conditions described in section 2.2.1 and ref. [7]. Spectra were analysed by least square fits to extract the spectroscopic quantities of interest. The line shape was represented by the parametrization of van der Straten *et al* (1988). The energies of vibrational states were assumed to be equidistant (harmonic approximation), or were given by equation (2). Thus, for each vibrational progression one or two free parameters were used to model the relative peak positions. All peak intensities were free parameters, or were chosen according to the linear coupling model (see [7]) where indicated. Besides that, the energy and intensity of the adiabatic peak, experimental broadening represented by a Gaussian, lifetime broadening and a linear background were used as fit parameters.

3.2.1. Methane - CH_4 The prototypical molecule for discussing vibrational excitation by inner shell photoionization is methane (CH_4). It was this molecule, for which vibrational structure in inner shell photoionization was first observed (Gelius *et al* 1974). The vibrationally resolved C 1s photoelectron spectrum of methane is shown in figure 4 [7]. Only totally symmetric modes can be excited. In this molecule of tetrahedral symmetry, there is only one such mode, namely the totally symmetric C-H bond stretch. Classically one can argue that due to the small mass of the hydrogen atoms involved, this mode is of high frequency, which translates to quantum mechanics as a large value of the vibrational quanta $\hbar\omega$. Our value is $\hbar\omega = 397(2)$ meV. The remaining results

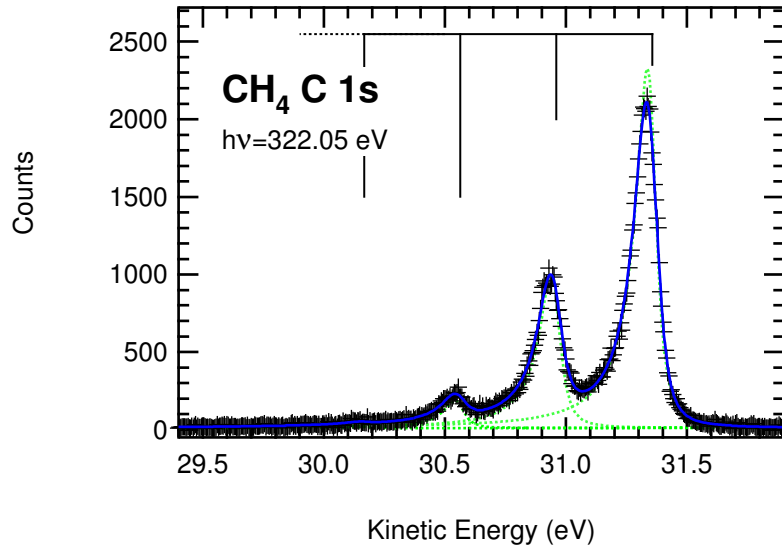


Figure 4. K -shell photoelectron spectrum of methane [7], measured with a total apparatus resolution of 44 meV. The solid line is the result of a least squares fit, broken lines are the individual components not convoluted by the apparatus function.

Table 2. Selected experimental (top panel) and theoretical values (bottom panel) for the intensity ratio of the first vibrationally excited final state in CH_4 C $1s$ photoionization to the vibrational ground state. A complete account of earlier work can be found in Karlsen and Børve (2000).

	$I(v' = 1)/I(v' = 0)$	Photon Energy
This work	0.430(7)	322 eV
Carroll <i>et al</i> (1999)	0.424(2)	330 eV
Köppe <i>et al</i> (1996)	0.435(10)	338 eV
Asplund <i>et al</i> (1985)	0.46	1481 eV (Al $K\alpha$)
Karlsen and Børve (2000a)	0.466	
Domcke and Cederbaum (1975)	0.47	
Asplund <i>et al</i> (1985)	0.34	

extracted from the spectrum in figure 4 are 0.430(7), 0.076(3), 0.0064(16) for the intensity ratios $I(v' = 1, 2, 3)/I(v' = 0)$ of the vibrationally excited states and 97.4(2.0) meV lifetime broadening. The anharmonicity contribution was found to vanish within the experimental accuracy. Our experimental values are in good agreement with results of Carroll *et al* (1999), which was one of the first studies that demonstrated the power of third generation synchrotron radiation for high resolution photoelectron spectroscopy.

Table 2 gives other experimental values for the degree of vibrational excitation in this ionization process, as displayed in the intensity ratio of the first vibrational excited state to the ground state. While there are no striking discrepancies between more recent experimental values, the spectrum recorded by Asplund *et al* (1985) with

a laboratory X-ray source at 1.5 keV photon energy shows a slightly larger intensity of the $v' = 1$ state. Although the apparatus resolution in this work cannot match the later synchrotron radiation experiments, the authors were well able to separate the $v' = 0, 1$ states. I therefore tend to consider this a valid difference, which would point to the possibility of changes in the vibrational coupling constant at energies higher than the currently accepted ‘sudden limit’ at approx. 40 eV above the ionization threshold. Not much more can be said about this, since no other studies with X-ray line sources or keV synchrotron radiation of a comparable quality are known to the author. Changes in the shape of vibrational bands at high kinetic energy of the photoelectron have been proposed from the photoelectron recoil to the remaining ion (Domcke and Cederbaum 1978, Gelmukhanov *et al* 2001). It is suggested that this effect leads to additional energy transferred into the vibrational degrees of freedom, but this has not been proven experimentally so far.

Comparing theory to experiment two different approaches, with Karlsen/Børve and Asplund *et al* on the one side, and Domcke/Cederbaum on the other side are to be discussed. The former two groups aimed at deriving the degree of vibrational excitation from a full calculation of the core ionized state, starting with a geometry optimization, then calculating the potential curves, the vibrational wavefunctions and the overlap integrals with the ground state numerically. The discrepancy of this approach with the experimental value in the study by Asplund *et al* (1985) is probably due to the inadequacy of the computational tools at that time. In contrast to this, Domcke and Cederbaum calculated the vibrational coupling constant from the gradient of the one-particle energy of the core electron at ground state equilibrium, modified to take relaxation into account by second order perturbation theory (see also Cederbaum and Domcke 1977). The nearly identical result of this calculation to the value of Karlsen and Børve can be rationalized by recalling that the vibrational excitation process occurs with the molecule being in its ground state equilibrium configuration. Therefore, it is computationally much more demanding to derive the vibrational coupling constant from a global calculation of the core ionized state than from a local expansion around the ground state equilibrium. A global description of the core ionized state will represent the photoelectron vibrational spectrum only when it correctly takes the anharmonicity of the potential curve into account on the full range of nuclear configurations.

As a result of the C 1s photoionization, shrinkage of the four C–H bonds by an equal amount occurs. Within the harmonic approximation, the C–H bond length of methane in the C 1s⁻¹ state can be determined from the experiment. The excursion in the totally symmetric normal coordinate is $Q_1 = 0.095(1) \text{ Å}(\text{amu})^{1/2}$ [7]. Since Q_1 is the normalized sum of four unit vectors, each pointing in the direction of one of the C–H bonds, the reduction in C–H bond length is $\Delta R_{CH} = -M_H^{-1/2}(Q_1/2) = -0.0474(4) \text{ Å}$, with M_H the hydrogen mass. The error reflects the inaccuracy of the input variables only. Different ‘experimental’ values for the change in bond length will be obtained, when other assumptions on the nature of the neutral and ionic potential curves are made. The most extensive calculation of Karlsen and Børve (2000) gives a

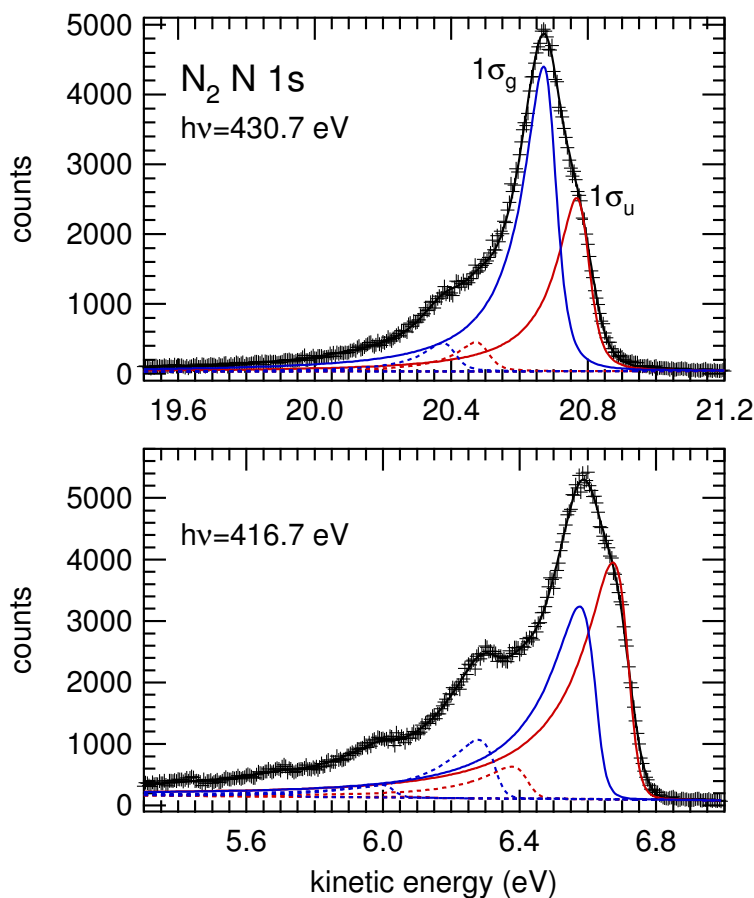


Figure 5. *K*-shell photoelectron spectrum of nitrogen [20], measured with a total apparatus resolution of 56(10) meV. Thick solid line: Result of a least squares fit, thin lines: Vibrational components of *g* and *u* final states, not convoluted with apparatus broadening (solid: $v' = 0$, broken: $v' = 1$).

value of -0.0482 \AA . To assess the significance of the difference between the calculation and the experimental value, the error that may be introduced by using the harmonic approximation for analysis of the experiment has to be quantified. Karlsen and Børve find this at 0.003 \AA . Thus, a geometry analysis from core level photoelectron spectra will only be able to discriminate between different modern theoretical values, when the accuracy of the measurement permits an analysis beyond the harmonic approximation.

3.2.2. Nitrogen - N_2 Nitrogen is a homonuclear diatomic molecule. Its electronic states therefore have *gerade* or *ungerade* symmetry with respect to inversion of the coordinate system. Although from quantum mechanics it is clear that this does apply to molecular core orbitals, it was for a long time not realized that the energy difference of *g* to *u* core hole states will be observable. The first experimental publication of the *g/u* energy difference in molecular core level ionization is by Kempgens *et al* (1997), where $C 1s^{-1}$

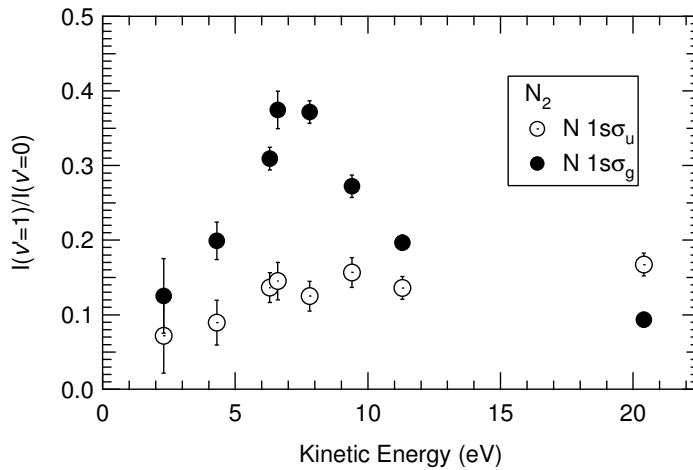


Figure 6. Intensity ratio of the first vibrationally excited final state in $N_2\ N\ 1s$ photoionization to the vibrational ground state [20].

states of ethyne (C_2H_2) were studied. In our work, the energy difference between *gerade* and *ungerade* states of $N_2^+\ 1s^{-1}$ is clearly visible (figure 5) [20]. We have measured its value as 97(3) eV, in good agreement with calculations by Kosugi (96.3 meV) and Thiel *et al* (101 meV) (Kosugi 2003, Thiel *et al* 2003).

Here, I will discuss the vibrational structure first. It will consist of two independent, incoherently overlapping progressions of the $N_2^+\ 1\sigma_g^{-1}$ and the $1\sigma_u^{-1}$ state. In this case, vibronic coupling cannot take place, since the only vibrational mode in N_2 is totally symmetric, and therefore cannot couple a *g* to a *u* state. The parameters of the two progressions have been extracted from the measured spectra assuming harmonic, identical vibrational spacings for both progressions. This deconvolution gives a vibrational spacing of 295(5) meV. The vibrational coupling constant (figure 6) is different for the two final states. For the $1\sigma_g^{-1}$ state, it displays a maximum at kinetic energies of 6.5-8 eV, which is at the onset of the $3\sigma_u^*$ shape resonance in the N_2 total photoabsorption cross section. This behaviour is similar to K-shell photoionization of CO. Due to dipole selection rules, only the *g* core orbital can couple to the shape resonance.

Our experimental results for the vibrational structure in $N_2\ N\ 1s$ photoionization are in good agreement with calculations by Thiel *et al* (2003). They find nearly identical vibrational spacings of 302.5 and 302.1 meV for the $N_2^+\ 1\sigma_g^{-1}$ and $1\sigma_u^{-1}$ state. $I(v' = 1)/I(v' = 0)$ is found asymptotically at 0.081 and 0.161, resp. The difference between the data points at highest kinetic energy in figure 6 is thus borne out by theory.

The cross section for $N_2\ 1s$ photoionization into the $N_2^+\ 1s^{-1}$ single hole state has been determined by Kempgens *et al* (1996) in absolute units. Using our data as input, we can partition their values into contributions of the *g* and *u* components. These data, which appeared in [20], have stimulated theoretical work on the $N_2\ 1s$ ionization process, since before that differences in inner shell ionization due to different symmetry of the ground state orbitals were not visible. Our experimental results are compared to three

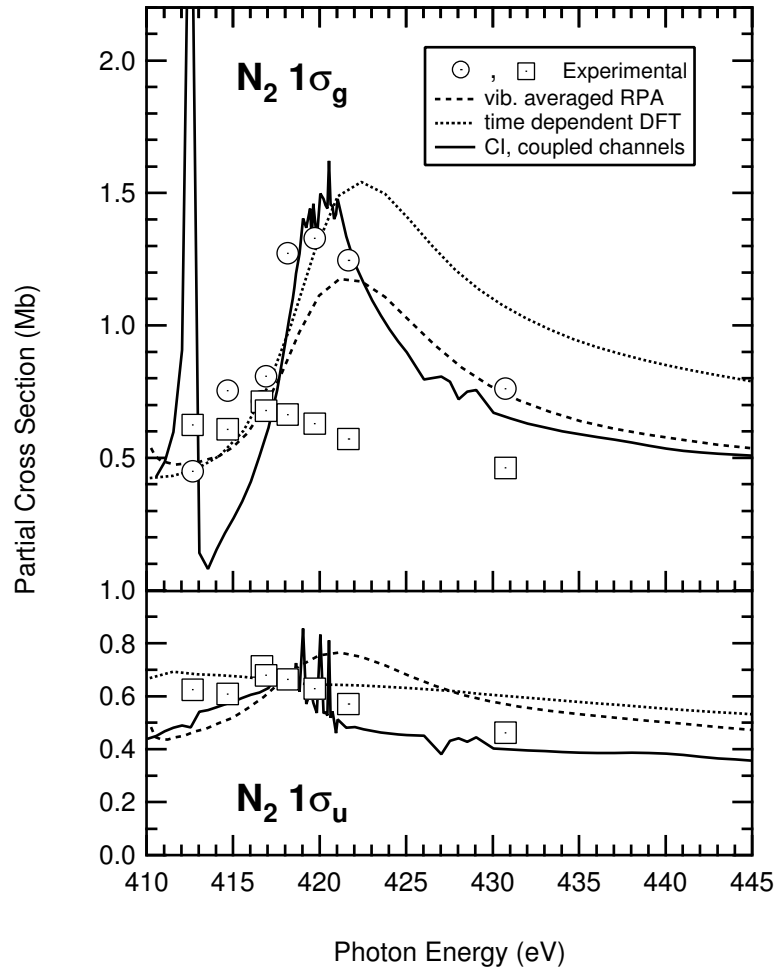


Figure 7. Partial cross sections for photoionization into the $N_2^+ 1\sigma_{g,u}^{-1}$ ionic states in absolute units. The sum of the experimental data has been normalized to the absolute single hole $N_2 1s$ photoionization cross section of Kempgens *et al* (1996). Experimental data (squares and circles) appeared in ref. [20]. Theoretical data are shown as lines. Solid lines: Lin and Lucchese (2002), dotted lines: Stener *et al* (2002), dashed lines: Semenov and Cherepkov (2002). The top panel shows results for ionization into the $1\sigma_g^{-1}$ state jointly with the experimental $1\sigma_u^{-1}$ data points for comparison, bottom panel is the $1\sigma_u^{-1}$ data.

recent theoretical data sets in figure 7.

It is interesting to discuss figure 7, since the three groups of authors use quite different methods for their calculations. The problems that every calculation of molecular photoionization has to master are 1. modeling of the photoelectron continuum wavefunction, which is oscillatory and unbounded, 2. account for electron correlation in the ground and final state, 3. account for relaxation of the orbitals due to the ionization and 4. interaction of different ionization channels. Some properties of the ionization process, such as total cross sections, can also be calculated by a response theory without explicit construction of the electron continuum. Let us see how these problems are dealt with

in the three works cited above.

Semenov and Cherepkov (2002) start with a relaxed core Hartree Fock (RCHF) calculation of the ionic state bound orbitals. In the field created by these orbitals, the continuum wavefunctions are calculated in prolate spheroidal coordinates, a special coordinate system adapted to two centre problems. From the full set of orbitals, dipole and Coulomb matrix elements are calculated. Then, electron correlation and interaction between different ionization channels is taken into account by calculating modified matrix elements as solutions of the RPA ('random phase approximation') equations. In the RPA method, a number of correlation terms neglected in the HF approximation can be taken into account. Averaging over different vibrational states was performed by repeating the calculations at different nuclear distances R . Lin and Lucchese (2002) use a variational method ('Schwinger variational principle') to self-consistently calculate the scattering wavefunction and the transition matrix between initial and final states. The radial part of the scattering wavefunction is expanded in a basis set of simpler bounded and oscillatory functions, while the angular part is taken care of by a single center expansion in spherical harmonics. It is possible to also include configuration interaction in the ground and the ionic final state, and interacting scattering channels in the continuum. The calculation shown in the figure is referred to as 10C-SCI II by the authors; besides the $1\sigma_u^{-1}$ and $1\sigma_g^{-1}$ states it includes all shake-up states arising from $ov - \pi_g$ excitations, where (ov) designates any of the outer valence orbitals. Stener *et al* (2002) give an example for the application of density functional (DFT) methods to molecular continuum states. In the ground state, DFT allows to treat more extended systems than the orbital based methods which have been mentioned. However the extension of DFT to the continuum is not straightforward. In the time dependent DFT (TD-DFT) adopted by the authors, the change in the density function is calculated self-consistently together with an effective potential, which includes the external photon field and Coulomb and exchange terms that incorporate the response of the density function to the external field. A basis set expansion in Slater type orbitals is necessary for the bound electrons, and the radial parts of the continuum states are represented by so-called B-splines. The angular part is taken care of by a one-center expansion. The coupling between g and u continuum channels was taken into account in the TD-DFT calculation. Both the calculations by Lin and Lucchese and Stener *et al* have been performed at fixed bond distances.

Comparison to the experimental values first of all shows that the position and strength of the shape resonance in the $1\sigma_g$ channel is predicted approximately correct by all three calculations discussed here. This represents a major improvement over earlier work (see discussion in Semenov and Cherepkov (2002) and Lin and Lucchese (2002)) and shows that the correct amount of target relaxation is included. The behaviour of the $1\sigma_u$ channel is much less pronounced, since on the single particle level the shape resonance cannot appear in this channel. Nevertheless its ionization is influenced by channel interaction, as can be seen from the failure of simpler calculations (not shown here) to represent its partial cross section. By interaction with the g channel, some

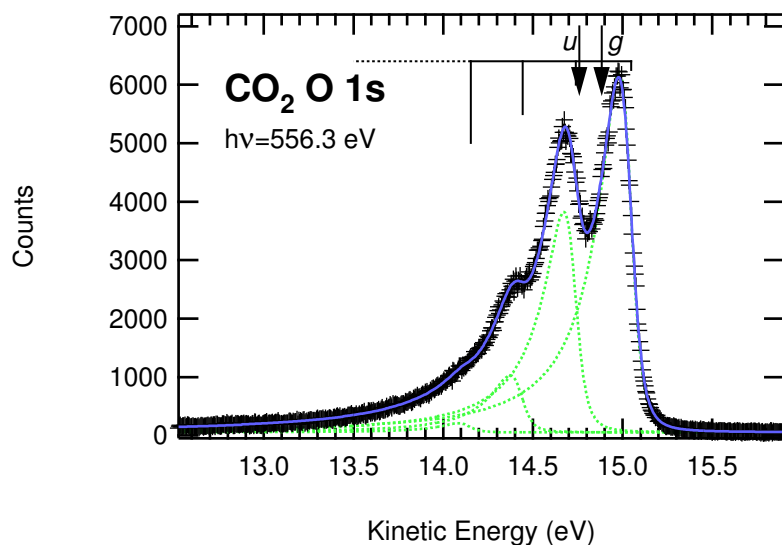


Figure 8. Oxygen K -shell photoelectron spectrum of carbon dioxide [7]. Arrows mark the positions of the ground state fundamental *gerade* and *ungerade* vibrations at 165 and 291 meV (Shimanouchi 1972), to be compared with the position of the $v' = 1$ excitation at -308 meV relative to the $0 - 0$ transition. Lines and symbols as in figure 4.

oscillator strength is transferred to the u (Semenov and Cherepkov) but the inclusion of shake-up states again changes this picture. When these final ionic state correlations are included, it is found that the amount of g - u channel interaction is less pronounced, but the interaction with shake-up states leads to larger calculated cross sections in the near threshold region (Lin and Lucchese). Moreover, numerous resonances are predicted. Experimental verification of these would require measurements at a dense set of photon energies; from the current experimental data their existence cannot be corroborated. The DFT results compare quite nicely to the experiment as well. With respect to these calculations, three things should be noted: 1. Interchannel coupling is included, the g/u coupling therefore is correctly shown to be weak, 2. shake-up channels are not included, and 3. one major motivation for developing this formalism is its applicability to larger systems. For the implementation discussed here, however, the representation of the continuum wavefunction by a one-centre expansion still is a bottleneck towards this aim.

3.2.3. Carbon Dioxide - CO_2 Carbon dioxide (CO_2) in its ground state is a linear molecule with conformation $O=C=O$. The vibrational structure of its carbon K -shell spectrum shows excitation of the symmetric stretch of the molecule, which is the expected behaviour (Kivimäki *et al* 1997).

The oxygen atomic $1s$ orbitals, due to the molecular symmetry, have to be arranged into *gerade* and *ungerade* combinations. Compared to the N_2 case discussed earlier, the difference of the ionization potentials for the CO_2 $1\sigma_{g,u}$ orbitals is much smaller, since

the overlap of the two constituent atomic orbitals is practically vanishing. A calculated value is 1.5 meV (Domcke and Cederbaum 1977). Nevertheless this small splitting has important consequences for the shape of the experimental spectrum.

The experimental spectrum shown in figure 8 has a vibrational spacing that compares much better to the frequency of the antisymmetric mode in the ground state, than to the symmetric mode or to the vibrational spacing observed in the CO₂ C 1s spectrum. Figure 8 is fully consistent with the first vibrationally resolved CO₂ O 1s spectrum reported by Kivimäki *et al* (1997). A similar, better resolved spectrum was somewhat later published by Carroll *et al* (2000). Since within the Born-Oppenheimer approximation the antisymmetric mode cannot be excited, this is an experimental proof for the interaction of electronic and vibrational structure (vibronic coupling). From the dominance of the antisymmetric mode and the fact that only the symmetric and the antisymmetric stretching mode can play a role, an approximate vibronic Hamiltonian at the ground state equilibrium configuration can be written (Domcke and Cederbaum 1977) [7], and from that it is qualitatively clear that the eigenfunctions of the ionic state correspond to localized rather than delocalized states. This has been termed dynamical localization. In photoionization experiments, localized and delocalized states provide two equivalent basis sets, in which all experiments can be properly described. However, in radiative X-ray scattering localized eigenstates lead to a different scattering spectrum than delocalized ones, and our conclusions on dynamical localization were impressively confirmed (Cesar *et al* 1996).

The above argument in favour of vibronic coupling does not preclude the excitation of a totally symmetric mode in competition with the antisymmetric mode. However, in CO₂ this is not observed. Dobrodey, Köppel and Cederbaum (1999) have calculated in great detail the potential surfaces of the CO₂ ground and O 1s ionized states and the vibrational spectrum they yield. They found that already the first excited state of the symmetric vibration, at 166 meV vibrational energy, has a Franck Condon factor of only 0.006. A fit of the experimental spectrum shown here, and the less well resolved experimental spectrum presented by Dobrodey *et al* (1999) do not show any evidence for this mode. Also in S 2p photoionization of CS₂ it was found that the spectrum is dominated by the antisymmetric mode (Siggel *et al* 1996).

Dobrodey *et al* found the equivalent core approximation to perform quite well, when it was used to construct the proper anharmonic potential surfaces and anharmonic spectra. The fit shown in figure 8 represents the spectrum by a single vibrational progression with $\hbar\omega = 318(3)$ meV and $\hbar\omega x_e = -4.9$ meV. The corresponding parameters extracted from the work of Dobrodey *et al*, taking into account only vibrations with prevalent σ_u symmetry, are $\hbar\omega = 321.5$ meV and $\hbar\omega x_e = -4.3$ meV. The first excited state is experimentally thus found at a spacing of 308 meV relative to the photoline of the ground state, compared to 307 meV in Kivimäki *et al* (1997). A comparison of the computed Franck Condon factors by Dobrodey *et al* (1999) to a somewhat worse resolved experimental spectrum at 581.8 eV photon energy showed perfect agreement as well.

4. Photoelectron circular dichroism in chiral molecules

In some materials two parallel beams of linearly polarized light with polarization direction perpendicular to each other propagate at different speed. This property is the physical basis of ‘optical activity’, the rotation of the polarization axis of a linearly polarized beam of light in a medium. It is also associated with ‘natural circular dichroism’ (CD), the difference in attenuation of circularly polarized light beams of opposite helicity. Molecules that show the aforementioned effects are called *chiral*. Chiral molecules were characterized by their optical effects in polarized light long before their geometrical structures were known. It is now established that each chiral molecule may exist in two different forms called *enantiomers*, which are mirror images of each other. While a pure solution of either enantiomer will show optical activity and circular dichroism, in a mixture of both forms (‘racemic mixture’) these effects will vanish. A lot of biologically important molecules are chiral. It is an astonishing and so far unexplained fact that biomolecules in nature always preferentially exist as only one of the two enantiomers.

The relative difference of the absorption coefficients in natural circular dichroism is small. Nevertheless, their measurement today is a standard laboratory technique. Typical CD measurements are carried out on solutes with concentrations in the mg/ml and pathlengths in the mm range. Then, the difference of the absorption coefficient between left- and right handed polarized light is 10^{-5} to 10^{-3} . The relative difference in the absorption coefficient might be as high as 0.02, but more commonly is in the 10^{-4} range. It follows that CD measurements are practically not possible on gaseous samples. This limits the range of frequencies that can be used for CD measurements because of absorption by the solvent. CD effects in the soft X-ray range, which were predicted theoretically, therefore only in one case could be confirmed experimentally (Turchini *et al* 2004).

In this section, the author will report about his experiments on a novel dichroic effect, which occurs in the partial differential photoionization cross section of unordered, chiral molecules. In contrast to recent experiments of other groups, here specifically the C 1s core levels are probed, which allows an easier connection of the effect to structural properties of the molecule.

4.1. Sign conventions

In experiments with circularly polarized light and handed samples it is important to have unique sign conventions. A state of light in which the electric field vector is rotating *counter-clockwise* in time when seen by an observer facing *towards* the light source will be called left circularly polarized. This (pure) polarization state is designated by a Stokes parameter S_3 of -1 . Both of these designations sometimes are called the ‘optical convention’. In quantum mechanical terms, photons in this state have a *positive* helicity. While the use of positive and negative helicity states seems to be unambiguous in the literature, in a number of works the terms left and right circularly polarized and/or the sign of the Stokes parameters are used in an opposite way.

The labelling conventions for enantiomers are well established. Absolute configurations can be designated using the labels R- and S-. These are applied according to the Cahn, Ingold, Prelog sequence rules describing the arrangement of groups about an asymmetric Carbon atom. These rules provide unambiguous assignment of absolute chiral configuration. Labels (−) and (+) are used to designate the direction of optical rotation (older alternatives were *d*-, *l*-). Since the latter are phenomenological, in this work they are only used to augment the R-, S- notation.

4.2. Theory of photoelectron circular dichroism

A circular dichroism in absorption is not possible in the electric dipole approximation. CD as outlined above is caused by an interference term between the electric and the magnetic dipole transition amplitude. The small magnitude of the effect follows from that. When angle resolved detection of the photoinduced reaction is possible, such as in photoelectron spectroscopy, symmetry restrictions are less stringent and it has been predicted that a circular dichroism of the angle resolved photoelectron intensity (Circular Dichroism in the Angular Distribution, CDAD) from an *unordered* sample of chiral molecules can occur already from electric dipole terms alone (Ritchie 1976). This effect must not be confused with CDAD from an *ordered* sample, *e.g.* in photoelectron spectroscopy of adsorbed molecules or of fixed-in-space molecules. Then, chirality may be induced by the experimental geometry and CDAD is even observable from non-chiral compounds. In the following, CDAD in the photoelectron angular distribution of an unordered sample will be designated as *photoelectron circular dichroism*.

The photoelectron angular distribution for purely circularly polarized light ($p = \pm 1$, designating positive and negative helicity of the photons) is

$$I_p(\theta) = \frac{\sigma}{4\pi} [1 + b_2 P_2(\cos \theta) + b_1^p P_1(\cos \theta)]. \quad (3)$$

Here, σ is the total cross section, θ the electron emission angle measured from the photon propagation vector to the electron momentum vector and P_i designates the Legendre polynomials, with $P_1(\cos \theta) = \cos \theta$. The b_1^p coefficient can occur only for chiral molecules. Its sign, but not its absolute value, changes upon change of the light helicity. b_2 does not depend on the helicity. It is related to the conventional β -parameter measured with linearly polarized light by $b_2 = -\beta/2$. The b_1^p coefficient also changes sign when the enantiomer of opposite handedness is probed.

Although this parametrization of the angular distribution was reported by Ritchie in 1976, and although a vast amount of data for the conventional β parameter was measured since then, even at the beginning of this century practically nothing was known about the other coefficient b_1^p . In 2000, numerical calculations appeared which suggested b_1^p will have a measurable absolute value for valence photoionization of some amino acids (Powis 2000). In a pioneering work, the first observation of photoelectron circular dichroism was reported in the valence photoionization of bromocamphor by Böwering *et al* (2001).

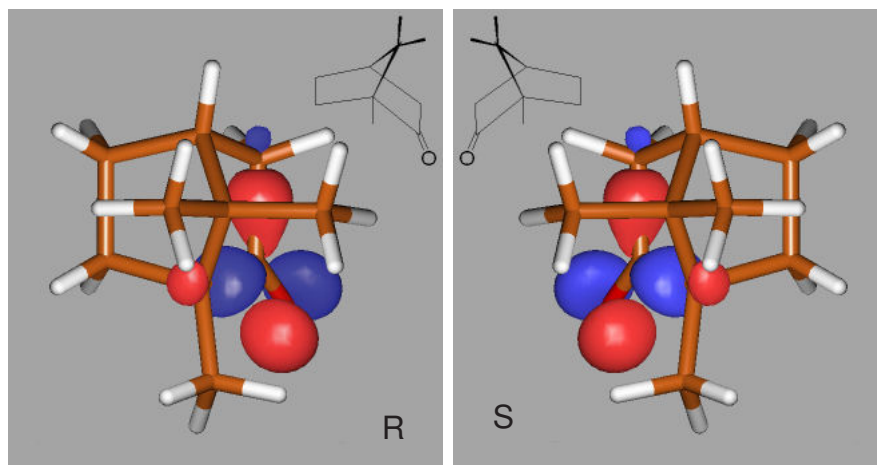


Figure 9. Conformations of (R)-(+)-Camphor and (S)-(-)-Camphor. A calculated isosurface of the HOMO (highest occupied molecular orbital) is shown near to the carbonyl group. Details of the calculation are in [17].

4.3. Photoelectron circular dichroism in *C* 1s photoemission of camphor

Camphor ($C_{10}H_{16}O$) is an organic hydrocarbon molecule with a chair-like conformation (figure 9). The ‘chair’ defines two spatial planes and a sense of direction, with respect to which the oxygen atom can be on the ‘left’ or ‘right’ hand side, giving two distinct enantiomers. High-resolution photoelectron spectra of the valence and core-level region of camphor have been recorded by our group [17]. These experiments were conducted in collaboration with the group of I. Powis, University of Nottingham, who participated in the measurements and provided all calculated results to be referred to in this chapter. For the experiments, commercial samples of camphor (Aldrich, enantiomeric purity > 95 %), which is a solid at room temperature, were admitted into the vacuum chamber via a gas line maintained at 80 °C. The vapour then entered a heated gas cell inside the main vacuum chamber where photoionization occurred [17].

In the outer valence region, due to the numerous molecular orbitals present in this binding energy region, the only distinct structure which is observable is from the HOMO. In the 10-16 eV binding energy range, about 20 orbitals overlap to a pattern, in which only small modulations are observable. This valence band structure was partly explained in [17]. In order to relate electron spectra to structural properties, it seemed nevertheless much more promising to concentrate on the region of core levels. A high resolution spectrum of the carbon core level region together with estimates for the respective binding energies from Hartree-Fock (HF) and density functional theory (DFT) calculations has been presented in [17] (see top panel of figure 10 for a spectrum measured with lower resolution). It was shown that the HF and DFT Koopman’s theorem estimates for the binding energy bracket the experimental values and lead to an unambiguous assignment with the smaller peak (experimental vertical ionization potential $I_{vert} = 292.34$ eV) being identified as the carbonyl C 1s ionization ($\underline{C}=\text{O}$ peak). All

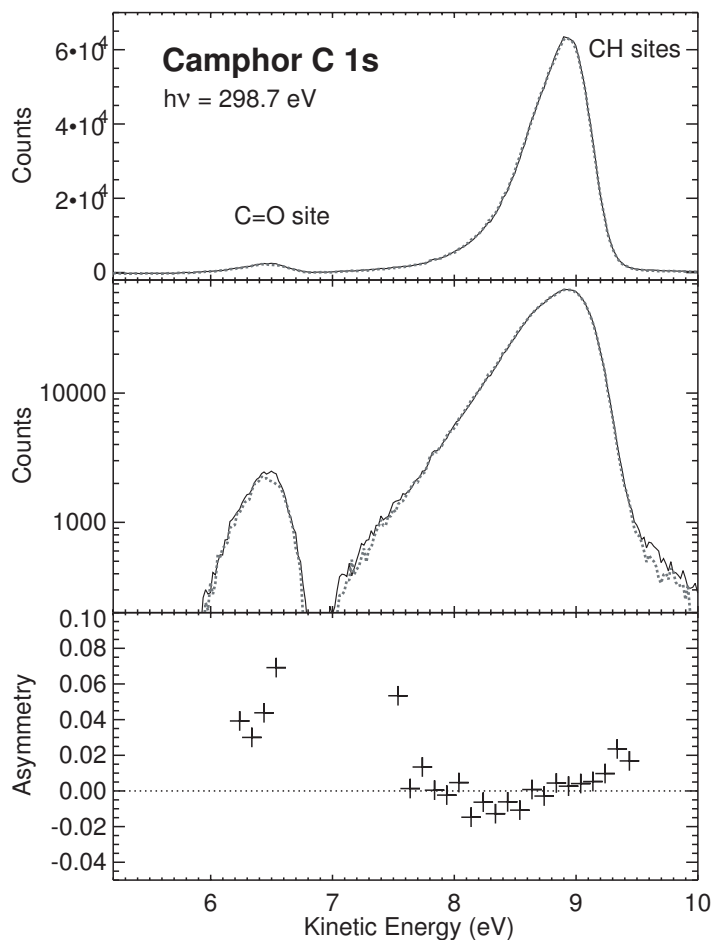


Figure 10. Top and middle panel: C 1s core level photoelectron spectrum of R-(+)-camphor. Bottom panel: Asymmetry calculated as the normalized difference between the signal for left and right handed circularly polarized light (solid and dotted lines). The chemical difference in binding energy for the carbonyl carbon can be easily resolved. Intensities have been normalized to yield a vanishing asymmetry for the signal of the C-H sites (see text).

other C 1s levels are largely overlapped under the main peak (experimental $I_{vert} = 289.86$ eV), though some structure can be discerned towards high energy on the experimental peak as might be expected from the calculated spread of shifts about the mean for these skeletal C peaks (C-H peaks). The experimental I_{vert} splitting (2.48 eV) is also in good accord with the mean splitting seen in the calculated eigenvalues. The C=O peak has been closely examined for any vibrational structure, but is essentially structureless, despite its having a FWHM (~ 300 meV) which is greater than the experimental resolution in ref. [17] (~ 90 meV) and greater than typical C 1s lifetimes which correspond to a width of 70-100 meV.

Photoelectron spectra of the C 1s region were recorded with circularly polarized light of both helicities at a number of photon energies as described in section 2.2.2. Comparing pairs of these spectra should reveal asymmetries proportional to the b_1^p coef-

ficient in the parametrization of the cross section, which is exclusive to chiral molecules. We define the asymmetry to be quoted in the following as

$$A := \frac{I_+ - I_-}{I_+ + I_-} \quad , \quad (4)$$

where $I_+(I_-)$ denotes the photoelectron intensity recorded under an angle of $\theta = 54.7^\circ$ with respect to the photon beam with positive (negative) helicity, which corresponds to left (right) circular polarization. Under this angle, the effect of the second Legendre polynomial in equation (3) vanishes and we have: $b_1^{+1} = A/\cos\theta$.

To arrive at meaningful results, normalization of the apparatus asymmetry resulting from slightly differing conditions in the sequential measurements is of crucial importance. In a simplified analysis of our data, we have assumed that the net asymmetry of the overlapping C-H lines is negligibly small, following a probable partial cancellation between opposing asymmetries arising on the different sites. We will return to this assumption below. Following this *ansatz* 15 % of the spectra, those displaying the largest apparent apparatus asymmetry of the C-H photoelectron lines, were rejected. Sequentially recorded spectra obtained with opposite helicity of the light were then normalized such that the asymmetry of the C-H C 1s lines is exactly zero.

Results of this analysis for one photon energy are displayed in figure 10. Although the difference between the signals for the both polarization types is not very strong, and can only be seen in a logarithmic plot (middle panel of figure 10) the asymmetry values derived for the C=O peak were significant and reproducible. In the following, values of the asymmetry integrated over the whole of the C=O peak will be discussed.

Experimental values for the asymmetry of the carbonyl C 1s line, thus derived, are displayed in figure 11. The figure gives clear evidence that this photoelectron line shows a non-vanishing asymmetry starting from the photoionization threshold and up to kinetic energies as high as 30 eV. Moreover it is clear that, as anticipated from the antisymmetry of the b_1^p coefficients with respect to reversal of the molecular helicity, the asymmetries of the two enantiomers mirror each other, with reversed signs.

We have also calculated photoionization matrix elements, and hence the parameters b_1^p , by a continuum multiple-scattering method with a local approximation for the exchange correlation (CMS-X α method). Three variants of such calculations are included in figure 11, together with a DFT based calculation by Di Tommaso *et al* (2004). Predicted asymmetries, $A(54.7^\circ)$, published in [9] are included in the upper panel of figure 11. For the kinetic energy region up to 35 eV, they reproduce the general trend of the experimental results quite reliably. The oscillatory structures in the calculated asymmetry at higher kinetic energies we have recently related to errors by truncation of the angular basis set, and an updated CMS-X α calculation included in the lower panel shows much less structure in the region between 35 and 50 eV, in agreement with experiment and with a recent calculation by time-dependent DFT.

In the variant designated as ‘corrected’ (broken lines in upper panel), the validity of the above experimental normalisation procedure has been tested by the calculation of the asymmetry for *each* C 1s orbital. Hence a cross section weighted average of all the

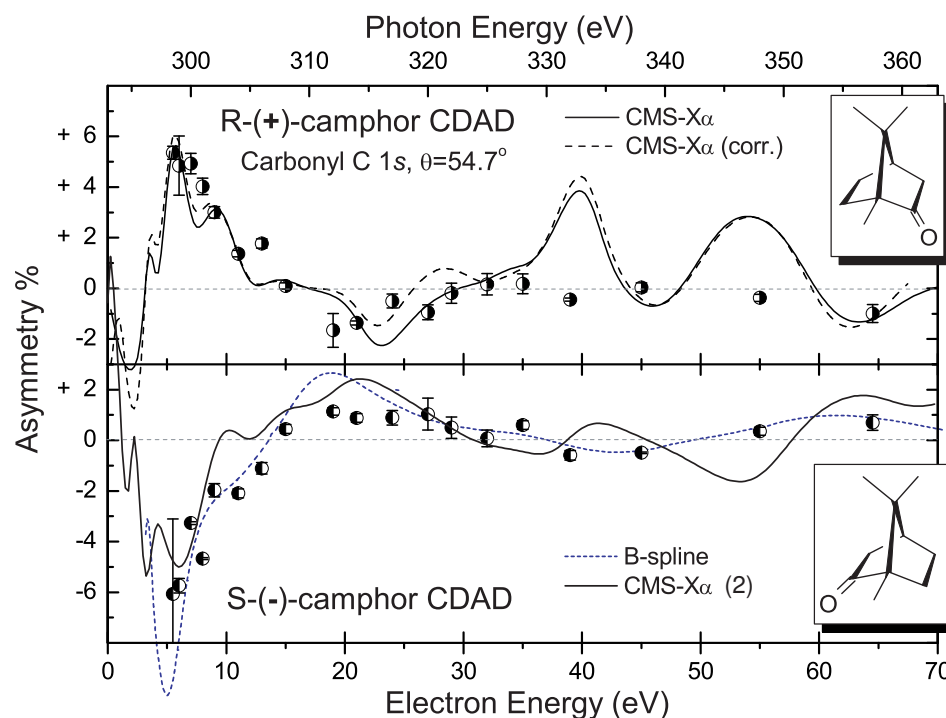


Figure 11. Normalized asymmetry of photoelectrons ejected from the carbonyl C 1s orbital of camphor by right-handed and left-handed circularly polarized light [9]. Error bars are derived from the variance of repeated measurements of the asymmetry. A scale error of 5 % relative to the asymmetry values (from the uncertainty in the degree of circular polarization) is not shown in the figure. The statistical error of a single measurement would typically be of the order of the symbol size. Solid lines in the upper panel display the result of a CMS-X α multiple-scattering calculation [9]. A modified calculation to estimate the error by normalizing data to vanishing $\underline{\text{C}}\text{-H}$ asymmetry is shown as a broken line (see text). For the other enantiomer both calculations have to be mirrored at the x -axis and are not presented for clarity. In the lower panel, two recent, unpublished calculations are shown. The solid curve is a CMS-X α calculation going to larger partial waves in the expansion of the continuum function (I. Powis 2004, private communication). Results of a DFT + B-spline based calculation (Di Tommaso *et al* 2004) are shown by broken lines. The latter has been done with an enhanced version of the programmes of Stener *et al* (2002) that have been discussed in the context of the N 1s photoelectron spectrum in section 3.2.2.

$\underline{\text{C}}\text{-H}$ levels was obtained which, as assumed, reduces to a relatively small residual effect due to cancellation of opposing asymmetries. A correction to the original calculation was then applied to mimic the consequences of the experimental normalisation procedure. The resulting correction differs little from the uncorrected curve apart from a small attenuation of the measured carbonyl C 1s asymmetry at some points, suggesting the experimental assumption of a zero net $\underline{\text{C}}\text{-H}$ electron asymmetry to be reasonably safe.

For a further verification we have re-calculated the experimental asymmetries from peak areas normalized directly against the photocurrent monitored at the beamline final refocussing mirror. This alternative treatment results in asymmetries for the $\underline{\text{C}}\text{=O}$ C 1s

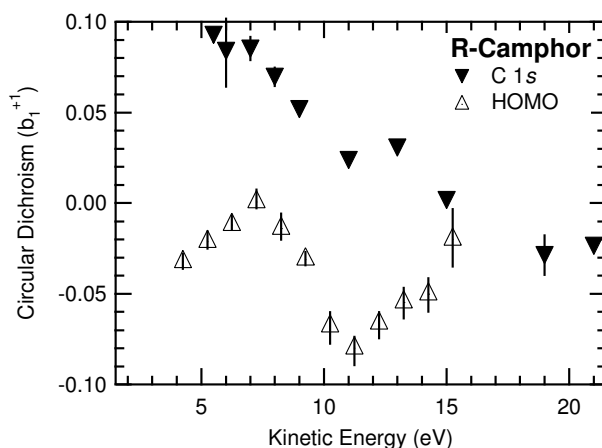


Figure 12. Dichroism (b_1^{+1}) of the photoelectron signal from the HOMO of camphor (Lischke *et al* 2004) compared to our data.

line which are clearly positive for the R-enantiomer and negative for the S-enantiomer at photon energies below 311 eV, but which change sign above this photon energy. This corroborates the trends seen in figure 11 although the larger scatter in the data generated by this approach obscures the smaller structures. Correspondingly the asymmetry of the 290.5 eV $\underline{\text{C}}\text{-H C } 1s$ line can now be estimated and, though again scattered, has an absolute value $\leq 2\%$ for more than 75% of the measurements examined, with no discernible systematic trends.

On inspection of the explicit expressions for b_1^p (section 4.2, Ritchie 1976) it is found that this unoriented molecule CDAD arises from interference between outgoing partial waves of adjacent orbital angular momentum ℓ values (i.e. a final state of indefinite parity). Now, the carbonyl inner shell orbital is a nearly pure C $1s$ orbital. The initial level is thus of well defined parity, rigorously localised and isolated from the chiral molecular potential – indeed it is identical for both enantiomers. The photoelectron circular dichroism we have observed can therefore be classified as a purely final-state effect, where the outgoing photoelectron partial waves lose their definite parity by scattering off the chiral molecular potential. It is therefore directly connected to the chiral geometrical structure of the molecule. This does not rule out that for delocalized orbitals an initial state effect can also contribute, as speculated by Böwering *et al* (2001).

Very recently, two reports on photoelectron circular dichroism in valence shell photoionization of camphor have been published (Garcia *et al* 2003, Lischke *et al* 2004). In the latter, the dichroism of the valence band of camphor is followed over a photon energy range of about 12 eV. If photoelectron circular dichroism indeed is a pure final state effect, it is reasonable to expect similar signals for the dichroism from the camphor $\underline{\text{C}}\text{=O C } 1s$ line and the HOMO, since the latter is localized at the C=O double bond. This comparison is shown in figure 12, where it can be seen that only the general trend of the data shows some qualitative agreement. One should note however that the

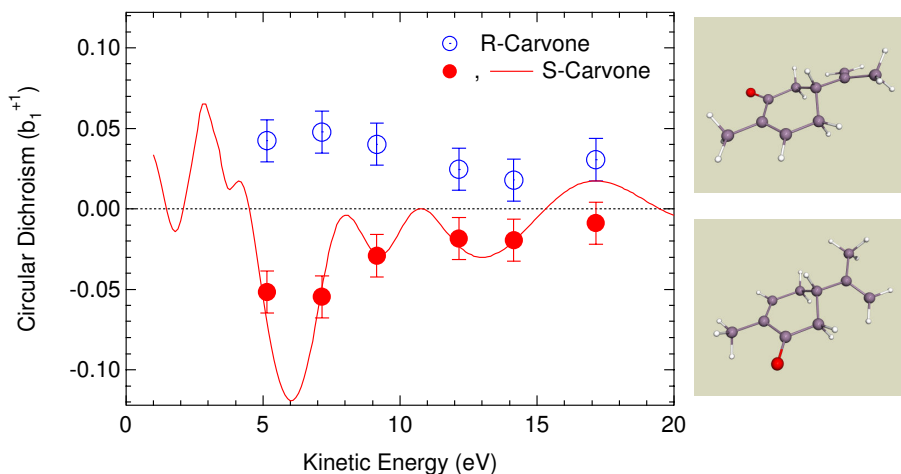


Figure 13. Dichroism (b_1^{+1}) of the photoelectron intensity from the carbonyl C $1s$ orbital of carvone together with data of an CMS- $X\alpha$ calculation (C. Harding, I. Powis, U. Hergenhahn *et al* 2004, to be published).

HOMO has a π character (figure 9), while the inner shell orbital is s . It seems plausible that these rather fundamental differences lead to a different interference pattern with the scattered photoelectron waves in the final state.

4.4. Photoelectron circular dichroism in C $1s$ photoemission of carvone

In order to generalize the results reported above on camphor the chiral molecule carvone ($C_{10}H_{14}O$) has been investigated recently. Carvone is a liquid that builds up a vapour pressure sufficient for photoelectron spectroscopy at temperatures of about 90 °C. The two enantiomers can be distinguished by their smell of spearmint (R-(–)-carvone) and of caraway seed (S-(+)-carvone), respectively.

Carbon K-shell photoelectron spectra of both enantiomers of carvone were recorded in the same geometry and with similar analyser settings as in the camphor measurements. However, a change of the photon beam helicity now was accomplished by switching between the two beams of the UE 56/2 twin undulator with a mechanical chopper (see section 2.2.2). A much better cancellation of apparatus asymmetries could thus be achieved. Asymmetries of the carbonyl C $1s$ line were calculated from

$$A = \frac{(I_{u,+}I_{d,+})^{1/2} - (I_{u,-}I_{d,-})^{1/2}}{(I_{u,+}I_{d,+})^{1/2} + (I_{u,-}I_{d,-})^{1/2}}. \quad (5)$$

The subscripts u and d designate signals from the upstream and downstream undulators, respectively, and the subscripts $+$ and $-$ designate left and right-handed circularly polarized light. Averaging over four spectra is necessary to achieve cancellation of the apparatus asymmetry from the dissimilar photon flux of the two undulators (the downstream undulator always gives a higher photon flux due to its larger solid angle seen at the experiment) and using the geometrical average of the pairs of equivalent spectra is necessary to achieve cancellation of unequal accumulated numbers of photons due to the

drop in ring current with time. The asymmetry of the two partial intensities can thus be determined with an accuracy of approx. ± 0.015 *without* use of an internal monitor. Unpublished results for the carbonyl C 1s line of both carvone enantiomers are shown in figure 13. Here, the geometrical factor of $\cos 54.7^\circ$ arising from the parametrization (3) was removed from the values in the graph. Again, a significant asymmetry of opposite sign in the two enantiomers is observed.

4.5. Summary

In the preceding section it has been shown that a significant difference of the angle-resolved photoelectron intensity of a chiral molecule ionized with circularly polarized light can be observed when the handedness of the ionizing radiation is reversed. Orientation of the sample is not a prerequisite for the occurrence of this effect. Its magnitude can well be in the percent range.

As an important consequence, the momentum transfer to the photoion will show an enantiomer selective anisotropy that corresponds to the anisotropy in the photoelectron angular emission pattern. It is thus conceivable that photoelectron circular dichroism can in future be used as a means of mechanical separation of the enantiomers of a racemic molecular mixture. This has not been achieved by other methods before.

The gas target required for measurement of photoelectron circular dichroism has a density of 10^{-3} to 10^{-4} mbar, and a spatial extension of roughly $1\ \mu\text{l}$. Obviously, with suitable methods for directed evaporation of the sample, very small amounts of material are sufficient for probing by photoelectron CD. As a future perspective, this effect can be developed into a laboratory technique that will be a useful complement to the solution based methods currently in common use.

5. Interatomic Coulombic Decay in weakly bonded systems

Double ionization of a weakly bonded system of identical atoms or molecules requires less energy than double ionization of the respective monomers. This is obvious, since in the extended system doubly ionized states with less Coulomb repulsion than in the monomer can be constructed, and it has been observed in numerous experiments *e.g.* in mass spectrometry of rare gas van-der-Waals clusters (*e.g.* Rühl *et al* 1992). However, it has gone for a long time unnoticed that in a lot of van-der-Waals and hydrogen bridge bonded clusters, the order of energy levels is such that the lowering of the double ionization threshold by cluster formation renders a large number of inner valence singly ionized states unstable against autoionization. In a pioneering work, Cederbaum *et al* in 1997 predicted autoionization of F $2s^{-1}$ states in $(\text{HF})_3$ and O $2s^{-1}$ states in $(\text{H}_2\text{O})_{2,3}$. This is not obvious, since this process consists of a direct transition from a localized inner-valence vacancy into a *delocalized* two-hole state. Hence this process is markedly different from the well known Auger decay, in which a deep inner shell hole undergoes a transition to a localized two-hole state, *i.e.* both final state vacancies are located at the site of the initial hole. For direct autoionization into delocalized two-hole states in weakly bonded systems, which is only possible by a simultaneous transition at two different sites of the system, thus the term *Intermolecular Coulombic Decay* (ICD) is now used[§].

§ Depending on the context, ICD may also designate *Interatomic* Coulombic Decay

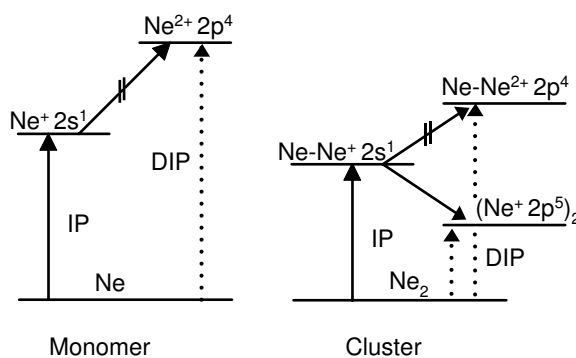


Figure 14. Sketch of the important energy levels in Ne and Ne_2 (not to scale) [13]. In Ne, a $2s$ vacancy cannot decay by an Auger process, because the transition from $\text{Ne}^+ 2s^1 2p^6$ to the final state $\text{Ne}^{2+} 2s^2 2p^4$ by electron emission would consume energy (left panel). For a Ne cluster the situation is different. In this case a $2s$ vacancy can relax from $\text{Ne}^+ 2s^1 2p^6$ to $(\text{Ne}^+ 2s^2 2p^5)_2$ by ICD. In the final state the two $\text{Ne}^+ 2s^2 2p^5$ sites in the cluster will have a significantly lower Coulomb repulsion than Ne^{2+} . Subsequently, the cluster will fragment by Coulomb explosion. The ionization potential (IP) and the double ionization potential (DIP) are given in the figure.

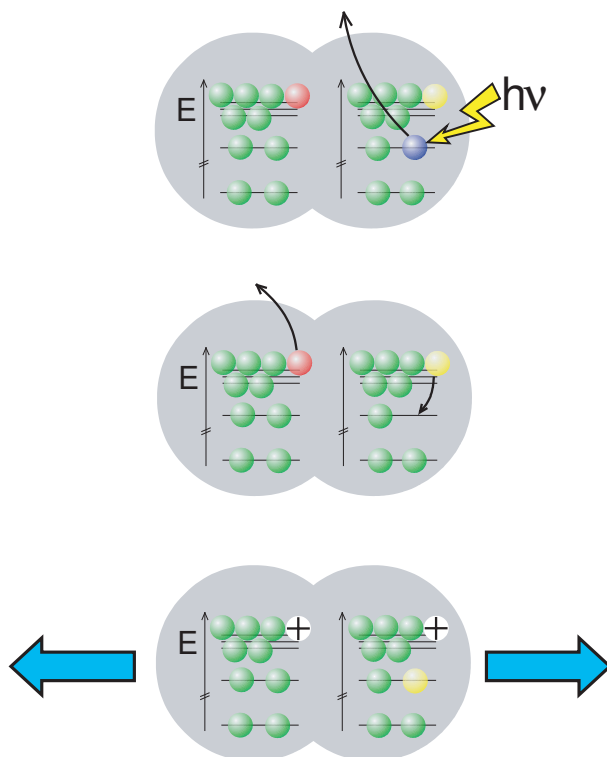


Figure 15. Sketch of the Interatomic Coulombic Decay of a Ne dimer. In the first step, a $2s^{-1}$ vacancy is created by photoionization. It decays by relaxation of a $2p$ outer valence electron into the hole. This goes along with an ultrafast energy transfer to a neighbouring site, where ionization of another $2p$ electron takes place. Eventually, the two opposing positive charges will initiate Coulomb explosion of the cluster. All of these aspects of ICD have been verified experimentally in recent work of the author: ICD electrons have been directly detected by electron spectroscopy [13], a measurement of the lifetime broadening has shown that ICD takes place on a fs timescale [4] and the dissociating fragments from the Ne dimer have been detected by momentum resolving ion spectroscopy [5].

5.1. The Interatomic/Intermolecular Coulombic Decay Process

The structure of energy levels which is a prerequisite for the existence of ICD is sketched in figure 14 using van-der-Waals clusters of Ne as an example. A pictorial representation of the decay process itself is given in figure 15.

When ICD is possible from a consideration of the respective state energies, the next question is whether it can compete against other relaxation mechanisms of ionized states, such as emission of ionic or neutral fragments. Although *a priori* it can be speculated that this will be the case since ICD is a purely electronic transition mechanism (\sim fs time scale) which does not involve the nuclear dynamics (\sim ps time scale) a rigorous answer to this question based on theoretical grounds is quite difficult to obtain. Using calculational methods tailored to the determination of the lifetime of excited states in extended systems, it was indeed predicted that IC decays of $2s^{-1}$ states in Ne van-der-Waals complexes will proceed on timescales ranging from 80 fs for Ne_2 to 2 fs for Ne_{13}

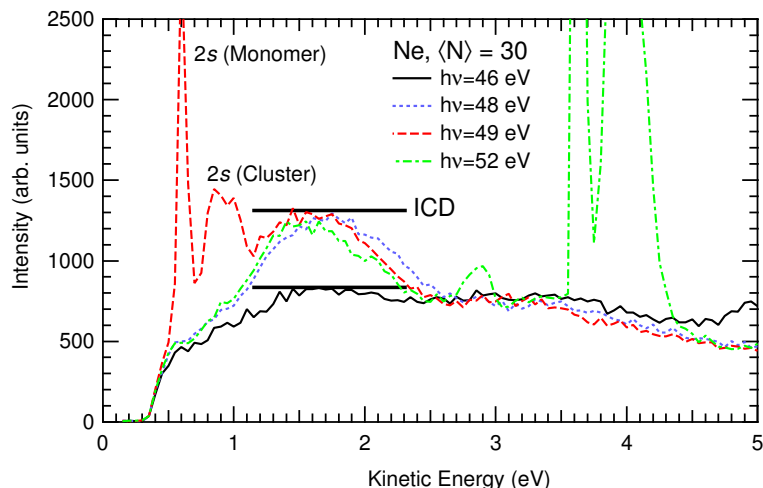


Figure 16. Electron spectra of Ne clusters around the threshold for 2s photoionization. An enhanced signal of low kinetic energy electrons between 1.2 and 2.5 eV can be seen at and above the 2s threshold of Ne clusters at 48.0 eV [4]. Its kinetic energy does not vary with photon energy. The kinetic energy of the 2s monomer and cluster main lines varies with photon energy; they can be seen in the spectra at 49 and 52 eV.

(Santra *et al* 2001), and will therefore foreclose all other decay channels thus far believed to be important in clusters.

5.2. ICD spectra of Ne clusters

To decide on these exciting predictions, Ne clusters excited by synchrotron radiation were investigated in our group in a set-up described in section 2.2.3. Figure 16 shows the kinetic energy distribution of electrons from Ne clusters exposed to synchrotron radiation of 46-52 eV photon energy. 48 eV is just the minimum energy required for 2s photoionization in a cluster [4], which is the initial excitation process for Ne ICD. At a photon energy of 49 eV, photoelectrons from the 2s level in Ne clusters and from the uncondensed part of the beam are visible in the figure. While the cluster peak is broadened and split into contributions from bulk and surface sites, the monomer peak is sharp and its width directly reflects the experimental broadening. Besides this feature, which is moving with photon energy, spectra recorded at 48 eV and above show a broad peak of electrons with kinetic energies between 1 and 2.5 eV, which is not present at lower photon energies, and disappears when the conditions for cluster formation are not met [13]. The position of this feature does not change with photon energy. This indicates that its origin is in ICD, since the kinetic energy of the emitted electrons is then given by the spacing of the levels involved in the decay only. Due to the broad distribution of cluster sizes, the energies of the ICD initial and final state levels become slightly modified, which leads to the appearance of a broad peak. Apart from that, also the nuclear dynamics of the final state contribute to the ICD peak width (Santra *et al* 2000, Scheit *et al* 2003).

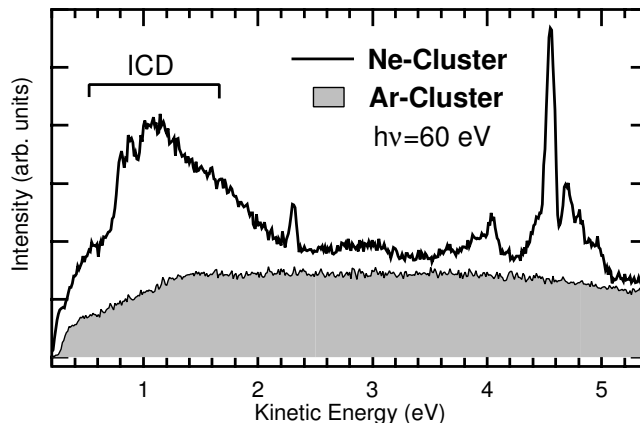


Figure 17. Comparison of the the low kinetic energy region of electron spectra from Ne clusters (solid line) and Ar clusters (shaded region) [13].

To add further evidence to this observation of low kinetic energy electrons, we have recorded electron spectra of photoexcited Ar and Ne clusters in an independent experiment under similar conditions as outlined above. In Ar, the positions of energy levels are somewhat different from Ne, with the consequence that ICD of Ar $3s^{-1}$ states is energetically not possible. We have determined IPs of 28.7 and 28.4 eV for surface and bulk $3s$ electrons, respectively, while the DIP is at 32 eV or higher, dependent on cluster size (Rühl *et al* 1992). Similar number densities of the gas targets were chosen. The photon energy was set below the threshold for photo double-ionization of a single Ne site (60.9 eV for Ne_2 and 62.53 eV for atomic Ne, see ref. [13] and references therein). Results are shown in figure 17. Inspection of the region below 2 eV kinetic energy in the Ar spectrum does not reveal the presence of any pronounced features.

Results comparable to figure 16 have been consistently obtained in independent measurements with a variety of experimental parameters, such as nozzle shape, nozzle diameter, nozzle temperature and stagnation pressure. Since the low kinetic energy electron peak around 1.6 eV only appears in condensed beams and only above the $2s$ threshold, it can be identified as originating in the emission of ICD electrons.

Additional information about the IC decay of the $2s^{-1}$ states can be obtained from an analysis of the primary photoelectron line. The mechanisms leading to the broad appearance of the ICD peak are absent for the photoline. It therefore seems possible to determine the IC decay rate from an analysis of the lifetime broadening of this line. We have carried out an experiment with this aim in collaboration with the group of O. Björneholm, University of Uppsala, at the Swedish synchrotron radiation source MAXlab. In figure 18 a photoelectron spectrum of the Ne $2s$ level of rather large clusters is shown. In the main part of the figure, the experimental spectrum is plotted together with a fit using symmetric Voigt functions, with free Lorentzian and Gaussian widths, to describe the cluster features. In the inset of the figure, the experimental spectrum is presented together with a fit using pure Gaussian line shapes for the cluster features.

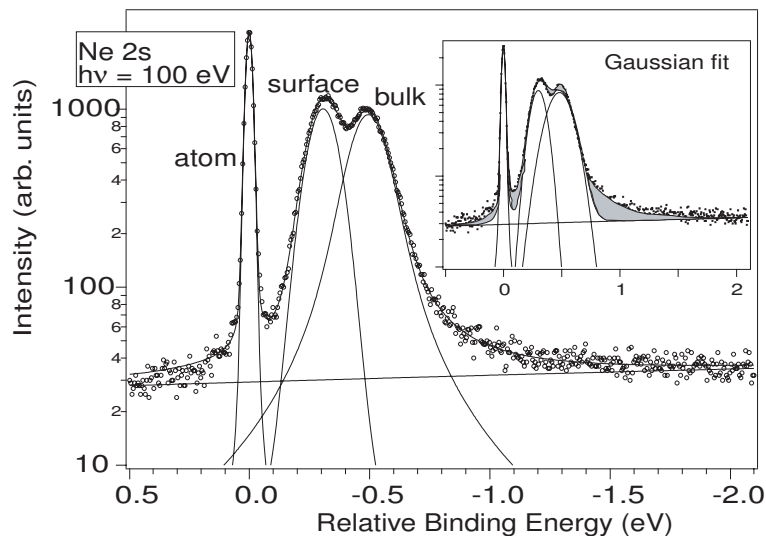


Figure 18. Photoelectron spectrum of the Ne 2s level of clusters with $\langle N \rangle \approx 900$. The spectrum is presented on a logarithmic intensity scale to emphasize the tails of the features. In the main part, a fit using a Voigt line profile is presented, and in the inset a Gaussian line profile is used. The regions which are not well described by the Gaussian line profile are shaded in the inset. A substantial Lorentzian component has to be taken into account to represent the bulk peak. The full width at half maximum of the atomic line, at 0 eV relative binding energy, is 30 meV, which is determined by the instrumental broadening.

An identical linear background has been subtracted in both cases. The spectra are presented on a logarithmic intensity scale to emphasize the tails of the cluster feature. Note that on a logarithmic scale, a Gaussian curve is a parabola, as can be seen in the inset. The Ne 2s level is a deep inner-valence level, and we do not expect it to show any appreciable effects of band broadening. We therefore represent the 2s cluster peaks by Voigt line profiles where the Lorentzian part corresponds to the lifetime broadening and the Gaussian part to other cluster inherent or experimental broadenings. The atomic peak, which has a full width at half maximum of 30 meV, has a Gaussian line shape due to instrumental broadening. A fit using a pure Gaussian shape for all peaks has some notable shortcomings: for instance, the tail towards lower binding energy cannot be modeled at all (see inset in figure 18). The best fit using Voigt line profiles has some interesting features: The surface part of the cluster feature is defined by the shoulder towards higher binding energy, and is best fit with a line profile which is close to a pure Gaussian, whereas the bulk component at lower binding energy is best fit using a considerable Lorentzian width to model the tail towards low binding energies. From the quantitative analysis of a series of spectra with different cluster sizes we obtain a Ne 2s hole lifetime of 6 ± 1 fs for bulk atoms in clusters larger than a few hundred atoms, and on average longer than 30 fs for surface atoms. These lifetimes are larger than those predicted for Ne₁₃ by Santra *et al* (2001), but they are of the same order of magnitude.

To arrive at more concise results, experiments on mass selected clusters are desir-

able. Since no practical method for the production of mass selected *neutral* clusters is known today, in the general case such experiments have not been carried out so far. In the particular case of the Ne dimer however, ICD leads to the production of two charged fragments which acquire momenta of equal magnitude but opposite direction during the Coulomb explosion of the Ne dimer dication produced in the decay. In a collaboration of the author with the group of R. Dörner, University of Frankfurt, ICD of the mass selected Ne dimer was investigated by recording electron-ion-ion coincidences. Magnitude and direction of the momenta of the ions were inferred by projecting them on a spatially resolving detector, similar to the technique described in the next section. Electrons were projected in the opposite direction, and where additionally confined to compact, cycloidal trajectories by a magnetic field aligned with the spectrometer axis. Together with the kinetic energy of the electron, this information was sufficient to uniquely identify events that represented $2s$ photoionization with subsequent IC decay. All predictions for ICD in Ne_2 (Santra *et al* 2000, Scheit *et al* 2003, 2004) were impressively corroborated [5].

5.3. ICD spectra of NeAr heteroclusters

For ICD to occur, the participating atoms and molecules not necessarily need to be of the same kind. In a heterogeneous systems AB, ICD to a mixed final state A^+B^+ is viable. These mixed system IC decays are of great potential interest, since the ICD rate is predicted to depend strongly on the nearest neighbour distance R (R^{-6} or faster, Averbukh *et al* 2004). Therefore, once a sound knowledge of the characteristics of IC decays in a number of systems exists, changes of the intensity and the spectral characteristics could be correlated to structural information on weakly bonded systems. In this respect, ICD resembles the well known Förster energy transfer (see next subsection).

As a step towards this application of ICD, we have investigated the decay of $\text{Ne } 2s^{-1}$ vacancy states in clusters created by a coexpansion of Ne and Ar. By a suitable choice of the mixing ratio and the nozzle temperature, a variety of clusters can be formed. Spectra have been recorded for mixed clusters with large (40 %) and small (10 %) Ar content, and as a cross check for a beam containing pure Ar clusters and uncondensed Ne monomers. An unpublished result of these studies is shown in figure 19. The following facts are clear from this figure: 1. only the Ne valence main lines show a significant (sharp) monomer line. This shows that most of the Ar condenses to clusters at the expansion conditions selected, but only part of the Ne. 2. Different from the data in figure 16, the Ne cluster line shows no splitting into bulk and surface components. The respective structure of the Ar cluster lines is less pronounced than in spectra of pure Ar clusters (not shown). We tentatively suggest that the clusters we have created consist of an Ar core surrounded by a mixed layer consisting of Ne and Ar. 3. From the area ratio of the normalized cluster main lines, a Ne content of the clusters of approx. 60 % can be calculated. (This estimate neglects inelastic losses of outgoing photoelectrons from the Ar core and the drop in analyser transmission for the Ar relative to the Ne

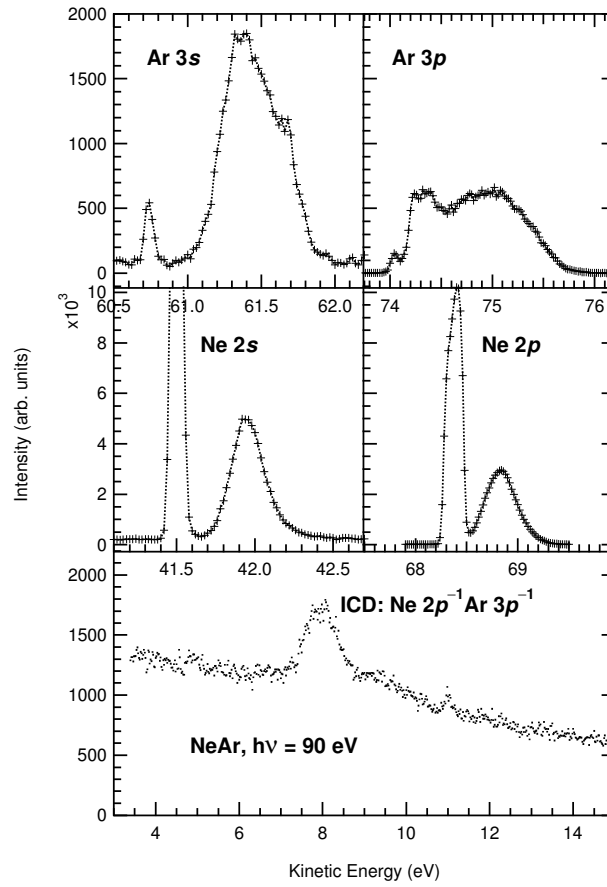


Figure 19. Low kinetic energy region and valence main lines of mixed NeAr clusters excited with a photon energy of 90 eV. The line at 7.8 eV kinetic results from emission of Ne $2s^{-1}$ vacancies into Ne $2p^{-1}$ Ar $3p^{-1}$ two hole states. The main line spectra have been normalized to the atomic $2s$ photoionization cross section. (S. Barth, S. Marburger, U. Hergenhahn *et al*, to be published)

lines. Both factors lead to an apparently smaller Ar content of the clusters. The figure can therefore be considered to be an upper limit of the Ne content.)

In the low kinetic energy region of the spectrum, a feature at a kinetic energy of about 7.8 eV appears. By recording additional spectra not shown here it has been checked that it appears at constant kinetic energy. Also, this line disappears in a beam of pure Ar clusters mixed with uncondensed Ne. Such conditions can be selected by raising the nozzle temperature slightly from a regime of mixed clusters. We therefore identify this peak as due to the ICD of Ne $2s^{-1}$ states into mixed delocalized Ne $2p^{-1}$ Ar $3p^{-1}$ dicationic states. With this assignment, the kinetic energy of the line is in satisfactory agreement with theory (Zobeley *et al* 2001).

5.4. Discussion and Summary

It has been shown that our experiments have resulted in unambiguous experimental proof for a direct autoionization of inner valence hole states in weakly bound systems into delocalized two-hole state. This process differs qualitatively from the well known Auger decay, and has been termed ICD (Interatomic or Intermolecular Coulombic Decay). Current experiments qualitatively and in part also quantitatively agree with theoretical predictions, which model ICD as an ultrafast energy transfer from the initially excited site to the neighbouring atom. In this subsection, I will put ICD into the correct perspective by comparing it to other non-local autoionization or energy transfer processes and by showing possible consequences and applications. I will first discuss an intuitive interpretation of the ICD process.

Although ICD is a new phenomenon, earlier discussions of non-local transition amplitudes in Auger decay in bulk matter bear some relation to it. In an early paper on this subject, Matthew and Komninos in 1975 derived the first explicit expression for the decay width due to interatomic transitions. Their result relates the decay rate of an inner shell vacancy A^+ to a mixed two hole state A^+B^+ with the valence photoionization cross section of B and the fluorescence decay rate for filling of the inner shell hole at A. The intuitive picture is that the decay at site A creates a virtual photon, which in turn ionizes site B. This picture captures some of the important features of ICD, most notably a strong (R^{-6}) dependence on the nearest neighbour distance and the increase of the importance of ICD for low kinetic energies of the emitted electron. Due to the limitations of the experimental data at that time it remained unclear whether the expression of Matthew and Komninos could be reconciled with experiments. In a recent experimental work it was used to rationalize the anomalous Si $2p$ lifetime broadening in SiF_4 (Thomas *et al* 2002). Although qualitatively this attempt has some credibility, recent theoretical work has shown that with respect to the application to ICD, the ‘virtual photon’ picture for most realistic systems has to be seriously modified. This is mainly because in the work of Matthew and Komninos a power law expansion for the Coulomb operator is used, which is only valid in the limit of asymptotically large bond lengths. Even in most van-der-Waals bonded systems this asymptotic range will not be reached, and often ICD rates will therefore be orders of magnitudes larger than predicted from the Matthew and Komninos formula (Averbukh *et al* 2004).

A resonant non-local autoionization process in bulk metal oxides some years ago was discovered and discussed as MARPE (Multi-Atom Resonant Photoemission). An objective discussion of this process was somewhat hampered by the fact that the original publication on MARPE in MnO (Kay *et al* 1998) grossly overestimated its importance because of an improperly calibrated detector response. Data remeasured by the same group show that after proper correction still a small amplification of *e.g.* the O $1s$ photoelectron intensity from MnO on an Mn $2p$ resonance remains (Kay *et al* 2001). Since MARPE is a resonant process taking place at photon energies in the soft X-ray range, Kay *et al* carry on by pointing out that ‘the connection between MARPE and

an interatomic Auger electron emission is primarily formal, since the same sorts of matrix elements are embedded in the expressions describing both. However, the overall processes are fundamentally different.'

Another well known process to be discussed in the context of energy transfer in weakly bonded systems is known as Resonance Energy Transfer (RET) or Förster Energy Transfer (Scholes 2003). RET can be observed *e.g.* by quenching of the fluorescence decay times after excitation of chromophores in biomolecules. It involves a donor and an acceptor group, both being parts of the same system, which can be an extended molecule or a solute. The process is initiated by photoexcitation of the donor site by absorption of a visible photon. The energy absorbed by it is then transferred to the acceptor site via dipole-dipole coupling. To ensure energy conservation, however, the nuclear dynamics has to be involved in the process as well. That is, different from ICD, RET is not a purely electronic process and the transfer times involved in it are typically orders of magnitude larger. Similar to ICD in the 'virtual photon' limit, the dependence on the nearest neighbour distance follows an R^{-6} law. This property of RET has been used as a tool to derive structural information on the donor-acceptor distance in biomolecules (Scholes 2003). Although a number of very important processes in nature and technology, *e.g.* light harvesting by chlorophyll molecules, involve RET, the conditions for it to take place are rather peculiar and are often not met. Compared to this, given an initial inner valence ionization ICD in mixed systems, as described above, is of a much more general nature.

6. Electron-ion coincidence spectroscopy with high energy resolution

Information on the dynamics induced by a photoionization process can often be revealed only by the detection of the photoelectron and/or secondary electrons in coincidence with the ionic fragments. The use of spectrometers which project the charged fragments onto one or two spatially resolving detectors have revolutionized this field, since they allow detection of the emitted particles within a large solid angle. By combination of electric fields with a time-of-flight (TOF) measurement, momentum reconstruction of the ionic fragments is possible. Reference [5], which has been discussed above, describes an experiment in which electrons and ions were detected with projecting spectrometers. Here, also the limitations of this technique become however apparent: Most notably, the energy resolution for the electrons bent onto corkscrew shaped trajectories by the magnetic fields is very limited. In ref. [5], it amounted to approx. 2 eV for Ne $2s$ photoelectrons of 10 eV kinetic energy. When a better energy resolution is needed or when electrons of a larger kinetic energy are to be detected, the use of projecting electron spectrometers has not been possible so far. Moreover, static electric fields cannot be used to detect the ions when a good energy resolution for the electrons is required.

In this closing section, I will describe results of an electron-ion coincidence measurement, in which detection of high kinetic energy electrons with high energy resolution and momentum resolved detection of the ionic fragments with 4π solid angle were simultaneously achieved. The experimental setup consisted of a hemispherical electron analyser modified in our group for use in coincidence measurements and a projecting ion spectrometer utilizing pulsed fields, which has been constructed by U. Becker and

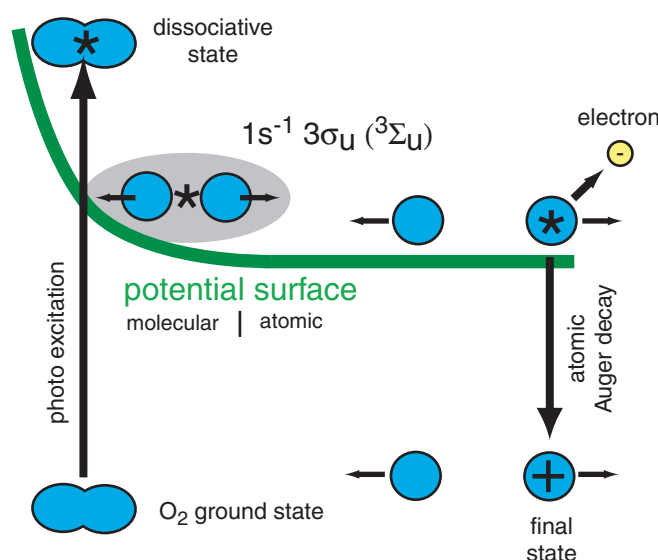


Figure 20. Schematic of the $O_2 1s \rightarrow 3\sigma_u^*$ resonant excitation and of the time evolution of the excited state. Due to the highly repulsive potential surface in the intermediate state, excited O^* -fragments may reach the atomic region before they decay.

coworkers (Fritz-Haber-Institut Berlin). Further technical details have been described (subsection 2.2.4, ref.s [6, 12]).

6.1. Intramolecular electron scattering and electron transfer in oxygen

The reaction we have studied is the fast dissociation of the free, core excited oxygen molecule (figure 20) after excitation of the $O_2\ 1s \rightarrow 3\sigma_u^*$ resonance. In this reaction, a large number of molecules dissociate into two oxygen atoms before the core excited state can relax (Caldwell *et al* 1994). Only after the two oxygen atoms have separated by several Ångströms, one of them emits an Auger electron. Björneholm *et al* discovered that the part of these electrons which has been emitted in the direction of the fragment ion, or antiparallel to it, shows a clear separation in energy by the momentum transfer from the dissociating atom. This has been termed a ‘Doppler shift’ (Björneholm *et al* 2000).

In the following I will concentrate on the autoionization electrons which are emitted in the atomic region of the potential curve. Since we have excited a homonuclear diatomic molecule, both, core hole and excited electron are the result of excitation from delocalized molecular orbitals of g or u symmetry. An atomic autoionization electron is eventually emitted from only one of the atoms. Björneholm *et al* recorded the energy of these atomic resonant Auger electrons and quantified their Doppler shift. Relating these energy shifts to the emission direction of the electrons with respect to the molecular axes however was only possible since, due to the dipole selection rules on a σ -type resonance, molecules with their axis oriented along the electric dipole vector of the radiation are preferentially excited. A more detailed insight into the decay process is possible when the axis orientation of each molecule is probed individually.

We have performed an experiment in which the fast autoionization electron emitted on the $O_2\ 1s \rightarrow 3\sigma_u^*$ resonance is detected in coincidence with the charged fragment. Time- and position-resolved detection of the ion allowed a reconstruction of the molecular axis direction for each event. A schematic of our apparatus and the kinematics of the charged particles is shown in figure 21. Fragments up to a kinetic energy of 10 eV were detected with 4π solid angle. We have determined the maximum of the fragment energy distribution as 3.5 ± 0.5 eV.

From the figure it is evident that in this setup the correlation between the sign of the momentum transfer to the electron and the axis direction of the molecule at the moment of fragmentation can be detected. We have analysed 52 000 coincidence events by calculating the axis direction from the hit position on the detector and the ion TOF using a manifold of simulated ion trajectories. From this, a two-dimensional map relating axis direction to electron energy can be drawn [6]. Restricting the electron emission angle now to forward or backward emission into a cone of 45° opening angle, the two-dimensional spectra can be integrated over the ion direction and we arrive at kinetic energy spectra of electrons emitted parallel and antiparallel to the ions, respectively. These results are shown in figure 22.

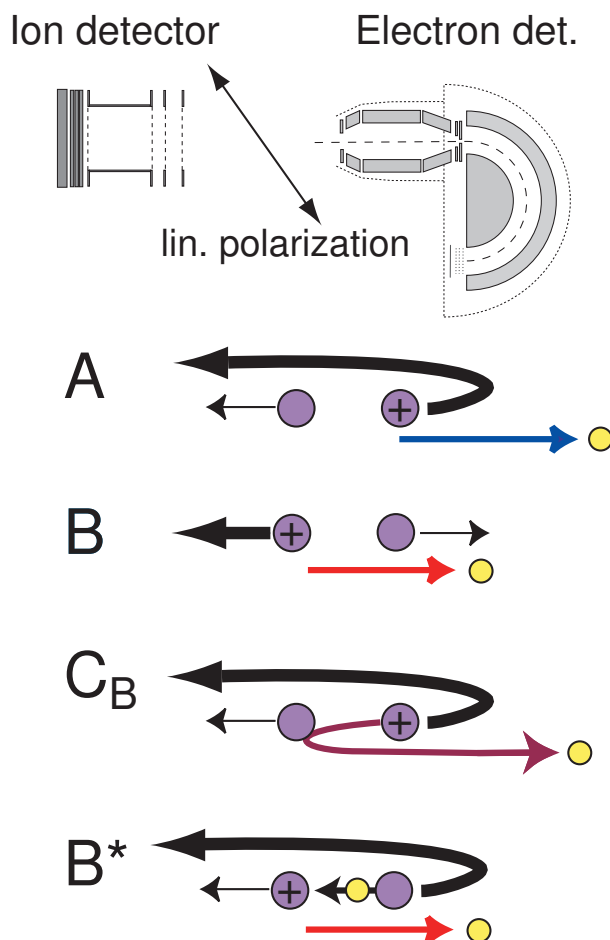


Figure 21. Experimental layout and kinematical correlation between electron and ion momenta. All ions, but only electrons emitted in the direction of the hemispherical analyzer are detected. Resonant Auger electrons having been emitted parallel to the ion momentum have a higher kinetic energy. The trajectory of the ion has to be reversed by the pulsed electric field triggered after detection of the electron, therefore these ions have a long time-of-flight (A). For emission of the electron opposite to the ion momentum, corresponding to lower kinetic energy, the ion is travelling towards the ion spectrometer initially, and has a short time-of-flight (B). Besides these processes, we have identified events in which backscattering of the resonant Auger electron at the neutral fragment occurs (C_B) and events, in which after the resonant Auger decay a negative charge is exchanged between the two fragments (B^*). Bold arrows designate which of the fragments is detected.

We have carried out a quantitative simulation of the spectra by a peak fit using the following assumptions:

1. Every spectrum contains four peaks, pertaining to direct emission into the detector (A or B, resp.), emission after scattering at the neutral fragment (C_B or C_F), emission into the detector with subsequent charge transfer between the fragments (B^* or A^*), and a scattered peak with subsequent charge transfer (C_B^* or C_F^*).
2. The area of the charge transfer peak is a constant fraction of the area of the respective

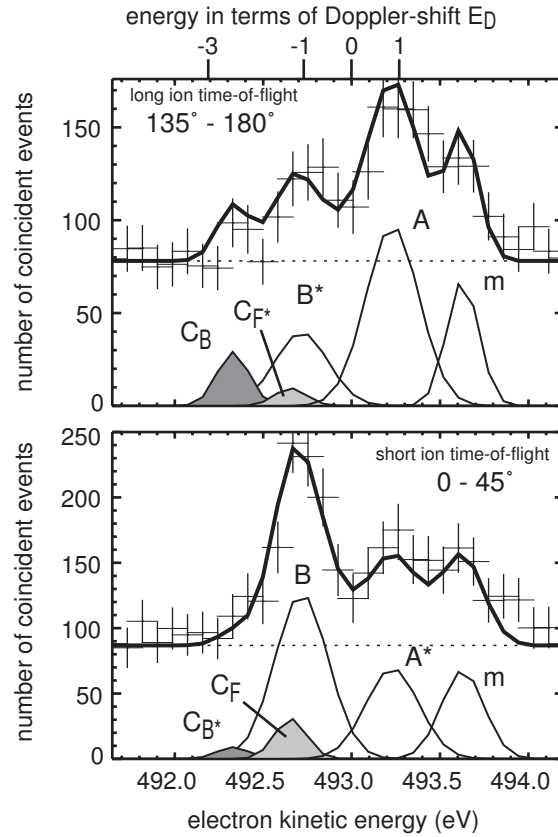


Figure 22. Kinetic energy spectra of electrons emitted parallel and antiparallel to the ions at relative angles of 135° - 180° and 0 - 45° , respectively [6]. The thick solid curves represent a fit result based on all available relative angles. Components A and B correspond to resonant Auger emission in the atomic region, components A* and B* to processes, in which after the electron emission a charge transfer to the ionic fragment occurs, components C_B and C_F to backward and forward scattering of resonant Auger electrons on the neutral fragment, and C_B^* and C_F^* to processes involving energy exchange by scattering and charge exchange between the fragments. The peak labelled ‘m’ we assign to decay into a molecular ionic state occurring before dissociation.

direct peaks, $A^* = cA$, $B^* = c'B$. The constants have been chosen differently in order to account for a possible anisotropy in the charge transfer after parallel and antiparallel emission of the autoionization electron. The difference between c and c' turns out to be less than 10 %.

3. The sum of redshifted and scattered electrons equals the number of blueshifted electrons, $A = B + C_B + C_F$.
4. The positions of all peaks in each angle selection are fixed to values calculated from a classical kinematical equation for the momentum transfer [6].
5. The peaks are modeled by Gaussians of constant width, and a constant background is added.
6. The intensity from molecular resonant Auger decay indicated as ‘m’, which appears

in all of the spectra, was modeled by an additional line of fixed kinetic energy.

Using a random walk method we thus arrive at the decomposition shown by the labelled areas in figure 22. In the fit, data for all electron relative emission angles have been used. Decompositions of a comparable quality for other angle selected subsets are not displayed here.

According to the simple picture for the process given by Björneholm *et al*, in each panel of figure 22 only one peak should appear. For electron emission roughly in the direction of the ion velocity this peak should be shifted towards higher kinetic energy, and vice-versa for emission of the electron opposite to the ion direction. These features, labelled A and B in figure 22, can indeed be identified, but additional structures are also present in both panels. Prominent is a peak (C_B) occurring for parallel (ion, electron) emission, but at a shift towards low kinetic energies that far exceeds the shift found for antiparallel emission. We attribute this peak to back-scattering of an electron at the neutral fragment atom. A classical kinematical calculation of the momentum transfer by backscattering gives an energy shift of three times the Doppler shift of the unscattered electrons, which is very close to the value we observe. The remaining energy difference can easily be explained by the fact that we record electrons with some distribution of relative emission angles.

Additional to this backscattered intensity, both panels show the presence of electrons with a Doppler shift that would fit to a direction of the ion momentum just opposite to what is observed (A^* and B^*). That is, the upper panel, where the ion has its original momentum in the direction of the electron detector, shows the presence of electrons with a Doppler shift characteristic for emission antiparallel to the ion velocity, that is in the direction of the ion spectrometer. Since our electron spectrometer only accepts electrons emitted within a small cone, these events cannot correspond to electrons emitted by the ion that is detected. We are therefore led to conclude that this additional intensity results from an exchange of a negative charge between the two oxygen fragments *after* the atomic resonant Auger electron has been emitted.

A consequence of the intramolecular scattering described here is that the fraction of electrons detected travelling in the direction of the ions is always larger than the fraction of electrons detected in the opposite direction. This intrinsic asymmetry with respect to emission into the inner and outer region of the molecule explains asymmetric electron emission behavior in diatomic homonuclear molecules, which for a long time was not understood (Golovin *et al* 1997, Lafosse *et al* 2001).

7. Outlook

Experiments reviewed in this section have been carried out at a third generation facility for production of synchrotron radiation. Meanwhile, the so-called fourth generation is under construction. These light sources known as Free Electron Lasers (FEL) will be based on linear accelerators, and will produce photon pulses with orders-of-magnitude higher flux within an orders-of-magnitude lower pulse duration. New experiments will become possible by that, such as pump-probe schemes with a fs optical laser, in which time development of an optically prepared state is probed by core level photoionization or detection of an ICD electron. Advanced coincidence detection techniques, as described in the preceding section, will certainly be useful for these experiments.

One important *caveat* should be noted: Due to technical reasons, the number of experiments that can be carried out at an FEL source is much smaller than the user time that can be provided by a conventional synchrotron radiation facility. Fortunately, at least in the author's opinion, the examples in this review show that we have just begun to explore the full potential of the sources we have today. Ample ideas for exciting experiments to be carried out in the near future can be found: In vibrationally resolved photoelectron spectroscopy, the invincible barrier of lifetime broadening can be beaten by going to highly resolved photoelectron-Auger electron coincidence spectroscopy. Since all channels for energy dissipation are then monitored, the resolution is only limited by the apparatus broadening which even today can be narrower than the lifetime broadening. In photoelectron circular dichroism, it will be very interesting to extend the experiments to biologically more important molecules, such as amino acids. Chirally selective destruction of these molecules by VUV sources for circular polarization has even been suggested as an extraterrestrial mechanism for creation of an enantiomeric excess, which might explain the homochirality of life on earth. With respect to ICD it is important that this effect has been predicted to be ubiquitous in weakly bonded systems, which includes hydrogen bridged aggregates, such as liquid water.

It is hoped that the experiments reviewed here will provide a good starting point for these future investigation.

Acknowledgements

First of all the author would like to thank Alex M. Bradshaw for his continuous interest in this work.

The experiments reported here would not have been possible without the help of my past and present coworkers Emma E. Rennie, Andy Rüdel, Oliver Kugeler, Simon Marburger, Silko Barth, Sanjeev Joshi and Volker Ulrich.

Further, the good experimental cooperation with Ivan Powis and his group, most notably Chris Harding, is acknowledged.

Uwe Becker and the members of his group, most notably Jens Viefhaus and Georg Prümper, have been very helpful by discussing uncounted scientific and technical questions while this work has been prepared.

The excellent support by the team of BESSY whenever problems occurred was very valuable for all measurements.

The quick start of the activity on cluster electron spectroscopy was greatly helped by Thomas Möller, who passed a lot of his expertise in this subject on to the author.

A lot about the theory of the processes investigated here was learnt in discussions with the Heidelberg group: Lorenz S. Cederbaum, Robin Santra, Horst Köppel and Jochen Schirmer.

The mechanical workshop of the Fritz-Haber-Institute has built even the most complicated designs with outstanding quality.

Partial funding of this work by the Deutsche Forschungsgemeinschaft through grants no. He 3060/3-3 and He 3060/4-1 is gratefully acknowledged.

Thanks are due to Karsten Horn for a critical reading of this manuscript.

References

- Asplund L, Gelius U, Hedman S, Helenelund K, Siegbahn K and Siegbahn P E M 1985 *J. Phys. B: Atom. Molec. Phys.* **18** 1569-79
- Averbukh V, Müller I B and Cederbaum L S 2004 *Phys. Rev. Lett.* **93** 263002
- Baltzer P, Karlsson L, Lundqvist M and Wannberg B 1993 *Rev. Sci. Instrum.* **64** 2179-89
- Becker U, Gessner O and Rüdel A 2000 *J. Electron Spectrosc. Relat. Phenom.* **108** 189-201
- Björneholm O, Bässler M, Ausmees A, Hjelte I, Feifel R, Wang H, Miron C, Piancastelli M N, Svensson S, Sorensen S L, Gel'mukhanov F and Ågren H 2000 *Phys. Rev. Lett.* **84** 2826-9
- Böwering N, Lischke T, Schmidtke B, Müller N, Khalil T and Heinzmann U 2001 *Phys. Rev. Lett.* **86** 1187-90
- Buckley C, Rarback H, Alforque R, Shu D, Ade H, Hellman S, Iskander N, Kirz J, Lindaas S, McNulty I, Oversluisen M, Tang E, Attwood D, DiGennaro R, Howells M, Jacobsen C, Vladimirovsky Y, Rothman S, Kern D and Sayre D 1989 *Rev. Sci. Instrum.* **60** 2444-7
- Caldwell C D, Schaphorst S J, Krause M O and Jiménez-Mier J 1994 *J. Electron Spectrosc. Relat. Phenom.* **67** 243-59
- Carroll T X, Berrah N, Bozek J, Hahne J, Kukk E, Sæthre L J and Thomas T D 1999 *Phys. Rev. A* **59** 3386-93
- Carroll T X, Hahne J, Thomas T D, Sæthre L J, Berrah N, Bozek J and Kukk E 2000 *Phys. Rev. A* **61** 042503
- Cederbaum L S and Domcke W 1977 *Advances in Chemical Physics* **36** 205-344
- Cederbaum L S, Zobeley J and Tarantelli F 1997 *Phys. Rev. Lett.* **79** 4778-81
- Cesar A, Gel'mukhanov F, Luo Y, Ågren H, Skytt P, Glans P, Guo J, Gunnelin K and Nordgren J 1996 *J. Chem. Phys.* **106** 3439-56; Erratum (1997) *J. Chem. Phys.* **107** 2699
- Di Tommaso D, Stener M and Decleva P 2004, private communication.
- Dobrodey N V, Köppel H and Cederbaum L S 1999 *Phys. Rev. A* **60** 1988-2001
- Domcke W and Cederbaum L S 1975 *Chem. Phys. Lett.* **31** 582-7
- 1977 *Chem. Phys.* **25** 189-96
- 1978 *J. Electron Spectrosc. Relat. Phenom.* **13** 161-73
- Feldhaus J, Erlebach W, Kilcoyne A L D, Randall K J and Schmidbauer M 1992 *Rev. Sci. Instrum.* **63** 1454-7
- Garcia G A, Nahon L, Lebech M, Houver J-C, Dowek D and Powis I 2003 *J. Chem. Phys.* **119** 8781-4
- Gelius U, Svensson S, Siegbahn H, Basilier E, Faxälv Å and Siegbahn K 1974 *Chem. Phys. Lett.* **28** 1-7
- Gel'mukhanov F, Salek P and Ågren H 2001 *Phys. Rev. A* **64** 012504
- Golovin A V, Heiser F, Quayle C J K, Morin P, Simon M, Gessner O, Guyon P M and Becker U 1997 *Phys. Rev. Lett.* **79** 4554-7
- Hemmers O, Wang H, Focke P, Sellin I A, Lindle D W, Arce J C, Sheehy J A and Langhoff P W 2001 *Phys. Rev. Lett.* **87** 273003
- Karlsen T and Børve K J 2000 *J. Chem. Phys.* **112** 7979-85
- Kay A, Arenholz E, Mun S, García de Abajo F J, Fadley C S, Denecke R, Hussain Z and Van Hove M A 1998 *Science* **281** 679-83
- Kay A W, García de Abajo F J, Yang S-H, Arenholz E, Mun B S, Mannella N, Hussain Z, Van Hove M A and Fadley C S 2001 *Phys. Rev. B* **63** 115119
- Kempgens B, Kivimäki A, Neeb M, Köppe H M, Bradshaw A M and Feldhaus J 1996 *J. Phys. B: At. Mol. Opt. Phys.* **29** 5389-402
- Kempgens B, Köppel H, Kivimäki A, Neeb M, Cederbaum L S and Bradshaw A M 1997 *Phys. Rev. Lett.* **79** 3617-20
- Kivimäki A, Kempgens B, Maier K, Köppe H M, Piancastelli M N, Neeb M and Bradshaw A M 1997 *Phys. Rev. Lett.* **79** 998-1001
- Köppe H M, Itchkawitz B S, Kilcoyne A L D, Feldhaus J, Kempgens B, Kivimäki A, Neeb M and

- Bradshaw A M 1996 *Phys. Rev. A* **53** 4120-6
- Kosugi N 2003 *Chem. Phys.* **289** 117-34
- Lafosse A, Brenot J C, Golovin A V, Guyon P M, Hoejrup K, Houver J C, Lebech M and Dowek D 2001 *J. Chem. Phys.* **114** 6605-17
- Lin P and Lucchese R R 2002 *J. Chem. Phys.* **117** 4348-60
- Lischke T, Böwering N, Schmidtke B, Müller N, Khalil T and Heinzmann U 2004 *Phys. Rev. A* **70** 022507
- Matthew J A D and Komninos Y 1975 *Surf. Sci.* **53** 716-25
- Powis I 2000 *J. Chem. Phys.* **112** 301-10; *J. Phys. Chem. A* **104** 878-82
- Randall K J, Feldhaus J, Erlebach W, Bradshaw A M, Eberhardt W, Xu Z, Ma Y and Johnson P D 1992 *Rev. Sci. Instrum.* **63** 1367-70
- Ritchie B 1976 *Phys. Rev. A* **13** 1411-5; *Phys. Rev. A* **14** 359-62
- Rühl E, Schmale C, Schmelz H C and Baumgärtel H 1992 *Chem. Phys. Lett.* **191** 430-4
- Santra R, Zobeley J, Cederbaum L S and Moiseyev N 2000 *Phys. Rev. Lett.* **85** 4490-3
- Santra R, Zobeley J and Cederbaum L S 2001 *Phys. Rev. B* **64** 245104
- Scheit S, Cederbaum L S and Meyer H-D 2003 *J. Chem. Phys.* **118** 2092-107
- Scheit S, Averbukh V, Meyer H-D, Moiseyev N, Santra R, Sommerfeld T, Zobeley J and Cederbaum L S 2004 *J. Chem. Phys.* **121** 8393-8
- Scholes G D 2003 *Ann. Rev. Phys. Chem.* **54** 57-87
- Semenov S K and Cherepkov N A 2002 *Phys. Rev. A* **66** 022708
- Senf F, Eggenstein F, Follath R, Hartlaub S, Lammert H, Noll T, Schmidt J S, Reichardt G, Schwarzkopf O, Weiss M, Zeschke T and Gudat W 2001 *Nucl. Instrum. Methods A* **467** 474-8
- Siggel M R F, Field C, Sæthre L J, Børve K J and Thomas T D 1996 *J. Chem. Phys.* **105** 9035-9
- Stener M, Fronzoni G and Decleva P 2002 *Chem. Phys. Lett.* **351** 469-74
- Thiel A, Schirmer J and Köppel H 2003 *J. Chem. Phys.* **119** 2088-101
- Thomas T D, Miron C, Wiesner K, Morin P, Carroll T X and Sæthre L J 2002 *Phys. Rev. Lett.* **89** 223001
- Turchini S, Zema N, Zennaro S, Alagna L, Stewart B, Peacock R D and Prosperi T 2004 *J. Am. Chem. Soc.* **126** 4532-3
- Weiss M R, Follath R, Sawhney K J S, Senf F, Bahrtdt J, Frentrop W, Gaupp A, Sasaki S, Scheer M, Mertins H-C, Abramoohn D, Schäfers F, Kuch W and Mahler W 2001 *Nucl. Instrum. Methods A* **467-468** 449-52
- van der Straten P, Morgenstern R and Niehaus A 1988 *Z. Phys. D* **8** 35-45
- Zobeley J, Santra R and Cederbaum L S 2001 *J. Chem. Phys.* **115** 5076-88

Articles marked by an * are included as reprints in the printed version of this work.

Publications by the author

- [1] G. Prümper, Y. Tamenori, A. De Fanis, U. Hergenhahn, M. Kitajima, M. Hoshino, H. Tanaka, and K. Ueda,
Ultrafast dissociation of F 1s excited SF₆ probed by electron ion momentum coincidence spectroscopy,
J. Phys. B **38**, 1 (2005).
- [2] N. Saito, D. Toffoli, R. R. Lucchese, M. Nagoshi, A. De Fanis, Y. Tamenori, M. Oura, H. Yamaoka, M. Kitajima, H. Tanaka, U. Hergenhahn, and K. Ueda,
Symmetry- and multiplet-resolved N 1s photoionization cross sections of the NO₂ molecule,
Phys. Rev. A **70**, 062724 (2004).
- [3] A. De Fanis, G. Prümper, U. Hergenhahn, M. Oura, M. Kitajima, T. Tanaka, H. Tanaka, S. Fritzsche, N. M. Kabachnik, and K. Ueda,
Photoelectron recapture as a tool for the spectroscopy of ionic Rydberg states,
Phys. Rev. A **70**, 040702 (2004).
- [4] * G. Öhrwall, M. Tchapyguine, M. Lundwall, R. Feifel, H. Bergersen, T. Rander, A. Lindblad, J. Schulz, S. Peredkov, S. Barth, S. Marburger, U. Hergenhahn, S. Svensson, and O. Björneholm,
Femtosecond interatomic coulombic decay in free neon clusters: Large lifetime differences between surface and bulk,
Phys. Rev. Lett. **93**, 173401 (2004), <http://link.aps.org/abstract/PRL/v93/e173401>
- [5] T. Jahnke, A. Czasch, M. S. Schöffler, S. Schössler, A. Knapp, M. Kász, J. Titze, C. Wimmer, K. Kreidi, R. E. Grisenti, A. Staudte, O. Jagutzki, U. Hergenhahn, H. Schmidt-Böcking, and R. Dörner,
Experimental observation of interatomic coulombic decay in neon dimers,
Phys. Rev. Lett. **93**, 163401 (2004).
- [6] * O. Kugeler, G. Prümper, R. Hentges, J. Viefhaus, D. Rolles, U. Becker, S. Marburger, and U. Hergenhahn,
Intramolecular electron scattering and electron transfer following autoionization in dissociating molecules,
Phys. Rev. Lett. **93**, 033002 (2004), <http://link.aps.org/abstract/PRL/v93/e033002>
- [7] * U. Hergenhahn,
Vibrational structure in inner shell photoionization of molecules,
J. Phys. B **37**, R89-R135 (2004), <http://stacks.iop.org/0953-4075/37/R89>
- [8] O. Kugeler, E. E. Rennie, A. Rüdél, M. Meyer, A. Marquette, and U. Hergenhahn,
N₂ valence photoionization below and above the 1s⁻¹ core ionization threshold,
J. Phys. B **37**, 1353-67 (2004).

- [9] * U. Hergenhahn, E. E. Rennie, O. Kugeler, S. Marburger, T. Lischke, I. Powis, and G. Garcia,
Photoelectron circular dichroism in core level ionization of randomly oriented pure enantiomers of the chiral molecule camphor,
J. Chem. Phys. **120**, 4553-6 (2004), <http://jcp.aip.org/jcp/>
- [10] I. Powis, E. E. Rennie, U. Hergenhahn, O. Kugeler, and R. Bussy-Socrate,
Investigation of the gas-phase amino acid Alanine by synchrotron radiation photoelectron spectroscopy,
J. Phys. Chem. A **107**, 25-34 (2003).
- [11] * S. P. Marburger, O. Kugeler, and U. Hergenhahn,
A molecular beam source for electron spectroscopy of clusters,
in Synchrotron Radiation Instrumentation: Eighth International Conference,
edited by T. Warwick *et al*, (American Institute of Physics, San Francisco, 2003),
AIP Conference Proceedings Vol. 705, p. 1114-6, <http://proceedings.aip.org/>
- [12] * O. Kugeler, S. Marburger, and U. Hergenhahn,
Calculation and measurement of the time-of-flight spread in a hemispherical electron energy analyser,
Rev. Sci. Instrum. **74**, 3955-61 (2003), <http://scitation.aip.org/>
- [13] * S. Marburger, O. Kugeler, U. Hergenhahn, and T. Möller,
Experimental evidence for Interatomic Coulombic Decay in Ne clusters,
Phys. Rev. Lett. **90**, 203401 (2003), <http://link.aps.org/abstract/PRL/v90/e203401>
- [14] U. Hergenhahn, A. Rüdél, K. Maier, A. M. Bradshaw, R. F. Fink, and A. T. Wen,
The resonant Auger spectra of formic acid, acetaldehyde, acetic acid and methyl formate,
Chem. Phys. **289**, 57-67 (2003).
- [15] E. E. Rennie, I. Powis, U. Hergenhahn, O. Kugeler, S. Marburger, and T. M. Watson,
Valence and C 1s core level photoelectron spectra of butan-2-ol,
J. Phys. Chem. A **106**, 12221-8 (2002).
- [16] E. E. Rennie, U. Hergenhahn, O. Kugeler, A. Rüdél, S. Marburger, and A. M. Bradshaw,
A core level photoionisation study of furan,
J. Chem. Phys. **117**, 6524-32 (2002).
- [17] E. E. Rennie, I. Powis, U. Hergenhahn, O. Kugeler, G. Garcia, T. Lischke, and S. Marburger,
Valence and C 1s core level photoelectron spectra of camphor,
J. Electron Spectrosc. Relat. Phenom. **125**, 197-203 (2002).
- [18] U. Hergenhahn, O. Kugeler, E. E. Rennie, A. Rüdél, and S. Marburger,
Vibrational excitation of C 1s ionized ethane,
Surface Reviews and Letters **9**, 13-9 (2002).

- [19] U. Hergenhahn, A. Kolmakov, M. Riedler, A. R. B. de Castro, O. Löffken, and T. Möller,
Observation of excitonic satellites in the photoelectron spectra of Ne and Ar clusters,
Chem. Phys. Lett. **351**, 235-41 (2002).
- [20] * U. Hergenhahn, O. Kugeler, A. Rüdel, E. E. Rennie, and A. M. Bradshaw,
Symmetry-selective observation of the N 1s shape resonance in N₂,
J. Phys. Chem. A **105**, 5704-8 (2001), <http://pubs.acs.org/>
- [21] G. Snell, U. Hergenhahn, N. Müller, M. Drescher, J. Viefhaus, U. Becker, and U. Heinzmann,
Study of xenon 4d, 5p, and 5s photoionization in the shape-resonance region using spin-resolved electron spectroscopy,
Phys. Rev. A **63**, 032712 (2001).
- [22] A. Kivimäki, U. Hergenhahn, B. Kempgens, R. Hentges, M. N. Piancastelli, K. Maier, A. Rüdel, J. J. Tulkki, and A. M. Bradshaw,
A near-threshold study of Xe 3d photoionization,
Phys. Rev. A **63**, 012716 (2001).
- [23] E. E. Rennie, B. Kempgens, H. M. Köppe, U. Hergenhahn, J. Feldhaus, B. S. Itchkawitz, A. L. D. Kilcoyne, A. Kivimäki, K. Maier, M. N. Piancastelli, M. Polcik, A. Rüdel, and A. M. Bradshaw,
A comprehensive photoabsorption, photoionisation and shake-up excitation study of the C 1s cross section of benzene,
J. Chem. Phys. **113**, 7362-75 (2000).
- [24] E. E. Rennie, H. M. Köppe, B. Kempgens, U. Hergenhahn, A. Kivimäki, K. Maier, M. Neeb, A. Rüdel, and A. M. Bradshaw,
Vibrational and shake-up excitations in the C 1s photoionisation of ethane and deuterated ethane,
J. Phys. B **32**, 2691-706 (1999).
- [25] M. N. Piancastelli, A. Kivimäki, B. Kempgens, K. Maier, A. Rüdel, U. Hergenhahn, and A. M. Bradshaw,
Constant Initial State (CIS) spectroscopy in the study of the decay of core-to-bound resonances in N₂,
J. Phys. B **32**, 2623-8 (1999).
- [26] G. Snell, M. Drescher, N. Müller, U. Heinzmann, U. Hergenhahn, and U. Becker,
Spin-resolved electron spectroscopy of the xenon N_{4,5}O_{2,3}O_{2,3} Auger lines,
J. Phys. B **32**, 2361-9 (1999).
- [27] G. Snell, B. Langer, M. Drescher, N. Müller, B. Zimmermann, U. Hergenhahn, J. Viefhaus, U. Heinzmann, and U. Becker,
Complete description of the Xe 4d photoionisation by spin-resolved photoelectron and Auger spectroscopy,
Phys. Rev. Lett. **82**, 2480-3 (1999).

- [28] U. Hergenhahn, G. Snell, M. Drescher, B. Schmidtke, N. Müller, U. Heinzmann, M. Wiedenhöft, and U. Becker,
Dynamically induced spin polarization of resonant Auger electrons,
Phys. Rev. Lett. **82**, 5020-3 (1999).
- [29] M. N. Piancastelli, B. Kempgens, U. Hergenhahn, A. Kivimäki, K. Maier, A. Rüdel, and A. M. Bradshaw,
Non-linear dispersion in resonant Auger decay of H_2O molecules,
Phys. Rev. A **59**, 1336-40 (1999).
- [30] M. N. Piancastelli, A. Kivimäki, B. Kempgens, M. Neeb, K. Maier, U. Hergenhahn, A. Rüdel, and A. M. Bradshaw,
Electron decay following the $N\ 1s \rightarrow \pi^$ excitation in N_2 studied under resonant Raman conditions*,
J. Electron Spectrosc. Relat. Phenom. **98-99**, 111-20 (1999).
- [31] B. Kempgens, H. M. Köppe, A. Kivimäki, M. Neeb, K. Maier, U. Hergenhahn, and A. M. Bradshaw,
On the correct identification of shape resonances in NEXAFS,
Surf. Sci. **425**, L376-L80 (1999).
- [32] M. Neeb, B. Kempgens, A. Kivimäki, H. M. Köppe, K. Maier, U. Hergenhahn, M. N. Piancastelli, A. Rüdel, and A. M. Bradshaw,
Vibrational fine structure on the core level photoelectron lines of small polyatomic molecules,
J. Electron Spectrosc. Relat. Phenom. **88-92**, 19-27 (1998).
- [33] K. Maier, A. Kivimäki, B. Kempgens, U. Hergenhahn, M. Neeb, A. Rüdel, M. N. Piancastelli, and A. M. Bradshaw,
The influence of multielectron excitations on the $O\ 1s$ photoionization in CO_2 ,
Phys. Rev. A **58**, 3654-60 (1998).
- [34] A. Kivimäki, K. Maier, U. Hergenhahn, M. N. Piancastelli, B. Kempgens, A. Rüdel, and A. M. Bradshaw,
Subnatural linewidths in core level excitation spectra,
Phys. Rev. Lett. **81**, 301-4 (1998).
- [35] A. Kivimäki, B. Kempgens, M. N. Piancastelli, M. Neeb, K. Maier, A. Rüdel, U. Hergenhahn, and A. M. Bradshaw,
Angle-Resolved electronic decay of the π^ , σ^* and Rydberg resonances below the $O\ K$ -Edge in O_2* ,
J. Electron Spectrosc. Relat. Phenom. **93**, 81-8 (1998).
- [36] B. Kempgens, K. Maier, A. Kivimäki, H. M. Köppe, M. Neeb, M. N. Piancastelli, U. Hergenhahn, and A. M. Bradshaw,
Vibrational excitation in $C\ 1s$ and $O\ 1s$ photoionization of CO ,
J. Phys. B **30**, L741-7 (1997).
- [37] B. Kempgens, H. M. Köppe, A. Kivimäki, M. Neeb, K. Maier, U. Hergenhahn, and A. M. Bradshaw,

- Reappraisal of the Existence of Shape Resonances in the Series C_2H_2 , C_2H_4 , and C_2H_6 ,*
Phys. Rev. Lett. **79**, 35-8 (1997).
- [38] U. Hergenhahn, S. B. Whitfield, J. Tulkki, F. Heiser, N. M. Kabachnik, B. Langer, and U. Becker,
Variation of the angular anisotropy in resonant Auger decay along the Mg $2p \rightarrow nl$ excitations,
Phys. Rev. A **55**, 2050-66 (1997).
- [39] G. Snell, M. Drescher, N. Müller, U. Heinzmann, U. Hergenhahn, J. Viefhaus, F. Heiser, U. Becker, and N. B. Brookes,
Spin polarized Auger electrons: The Xe $M_{4,5}N_{4,5}N_{4,5}$ case,
Phys. Rev. Lett. **76**, 3923-6 (1996).
- [40] A. Menzel, S. Benzaid, M. O. Krause, C. D. Caldwell, U. Hergenhahn, and M. Bissen,
Natural widths in open-shell atoms: The K absorption spectrum of atomic oxygen,
Phys. Rev. A **54**, R991-4 (1996).
- [41] T. Liebsch, O. Plotzke, R. Hentges, A. Hempelmann, U. Hergenhahn, F. Heiser, J. Viefhaus, U. Becker, and Y. Xu,
Photoelectron spectroscopy of free fullerenes,
J. Electron Spectrosc. Relat. Phenom. **79**, 419-22 (1996).
- [42] F. Heiser, O. Gessner, U. Hergenhahn, J. Viefhaus, K. Wieliczek, N. Saito, and U. Becker,
Photoelectron spectroscopy on oriented molecules,
J. Electron Spectrosc. Relat. Phenom. **79**, 415-7 (1996).
- [43] N. Müller, R. David, G. Snell, R. Kuntze, M. Drescher, N. Böwering, P. Stoppmanns, S.-W. Yu, U. Heinzmann, J. Viefhaus, U. Hergenhahn, and U. Becker,
Spin resolved Auger electron spectroscopy after photoexcitation with circularly polarized radiation from the BESSY crossed undulator,
J. Electron Spectrosc. Relat. Phenom. **72**, 187-93 (1995).
- [44] T. Liebsch, O. Plotzke, F. Heiser, U. Hergenhahn, O. Hemmers, R. Wehlitz, J. Viefhaus, B. Langer, S. B. Whitfield, and U. Becker,
Angle-resolved photoelectron spectroscopy of C_{60} ,
Phys. Rev. A **52**, 457-64 (1995).
- [45] U. Hergenhahn and U. Becker,
Angular distribution and spin-polarisation of Auger electrons,
J. Electron Spectrosc. Relat. Phenom. **76**, 225-8 (1995).
- [46] U. Hergenhahn and U. Becker,
Angular distribution in resonant Auger decay of atoms and molecules,
J. Electron Spectrosc. Relat. Phenom. **72**, 243-7 (1995).

- [47] S. B. Whitfield, U. Hergenhahn, N. M. Kabachnik, B. Langer, J. Tulkki, and U. Becker,
Angular anisotropy in the resonant Auger decay of 2p-photoexcited Mg,
Phys. Rev. A **50**, R3569-72 (1994).
- [48] B. Lohmann, U. Hergenhahn, and N. M. Kabachnik,
Spin polarization of Auger electrons from noble gases after photoionization with circularly polarized light,
J. Phys. B **26**, 3327-38 (1993).
- [49] U. Hergenhahn, B. Lohmann, N. M. Kabachnik, and U. Becker,
Angular anisotropy in the Auger decays of resonantly excited Kr $3d_{5/2}^{-1} 5p$ and Xe $4d_{5/2}^{-1} 6p$ states,
J. Phys. B **26**, L117-21 (1993).
- [50] F. Heiser, U. Hergenhahn, J. Viehhaus, K. Wieliczek, and U. Becker,
High resolution threshold photoelectron spectra of neon and argon in the valence satellite region,
J. Electron Spectrosc. Relat. Phenom. **60**, 337-49 (1992).
- [51] U. Hergenhahn, N. M. Kabachnik, and B. Lohmann,
Angular distribution in resonant Auger decay,
J. Phys. B **24**, 4759-73 (1991).

Invited, non-refereed publications

- [52] S. Marburger, O. Kugeler, and U. Hergenhahn,
How to excite your neighbour? Try ICD!,
BESSY Highlights 2003, 10-1 (2004).
- [53] G. Prümper, O. Kugeler, U. Hergenhahn, S. Marburger, D. Rolles, F. Burmeister, J. Viehhaus, R. Hentges, S. Cvejanovic, and U. Becker,
Ping-pong with ions and electrons: O₂ can do,
BESSY Highlights 2002, 22-3 (2003).
- [54] N. B. Brookes, G. Snell, M. Drescher, N. Müller, U. Heinzmann, F. Heiser, U. Hergenhahn, J. Viehhaus, R. Hentges, O. Gessner, and U. Becker,
Photoionization using circularly polarized soft X-rays,
ESRF Newsletter **24**, 17-9 (1995).